Astronomy & Astrophysics manuscript no. survey_co_article_arxiv
December 21, 2016
©ESO 2016

The hybrid disks: a search and study to better understand evolution of disks.

J. Péricaud[1,2], E. Di Folco[1,2], A. Dutrey[1,2], S. Guilloteau[1,2], and V. Piétu[3]

[1] Univ. Bordeaux, LAB, UMR 5804, F-33615, Pessac, France
[2] CNRS, LAB, UMR 5804, F-33615, Pessac, France
[3] IRAM, 300 rue de la piscine, F-38406 Saint Martin d'Hères, France.

Received July 22, 2016; accepted December 1, 2016

arXiv:1612.06582v1 [astro-ph.SR] 20 Dec 2016

ABSTRACT

Context. The increased sensitivity of millimeter-wave facilities now makes possible the detection of low amounts of gas in debris disks. Some of the gas-rich debris disks harbor peculiar properties, with possible pristine gas and secondary generated dust. The origin of the gas in these hybrid disks is strongly debated and the current sample is too sparse to understand this phenomenon.
Aims. More detections are necessary to increase the statistics on this population. Lying at the final stages of evolution of proto-planetary disks and at the beginning of the debris disk phase, these objects could provide new insight into the processes involved in the making of planetary systems.
Methods. We carried out a deep survey of the CO J=2→1 and CO J=3→2 lines with the *APEX* and *IRAM* radiotelescopes in young debris disks selected according to hybrid disk properties. The survey is complemented with a bibliographic study of the ratio between the emission of the gas and the continuum (S_{CO}/F_{cont}) in CTTS, Herbig Ae, WTTS, hybrid, and debris disks.
Results. Our sub-mm survey comprises 25 stars, including 17 new targets, and we increase the sensitivity limit by a factor 2 on eight sources compared to similar published studies. We report a $4\,\sigma$ tentative detection of a double-peaked CO J=2→1 line around HD 23642; an eclipsing binary located in the Pleiades. We also reveal a correlation between the emission of the CO gas and the dust continuum from CTTS, Herbig Ae and few debris disks. The observed trend of the gas to dust flux ratio suggests a concurrent dissipation of the dust and gas components. Hybrid disks systematically lie above this trend, suggesting that these systems may witness a transient phase, when the dust has evolved more rapidly than the gas, with a flux ratio S_{CO}/F_{cont} enhanced by a factor of between 10 and 100 compared to standard (proto-)planetary disks.

Key words. stars: circumstellar matter – proto-planetary disks – radio lines: stars

1. Introduction

The scenarios of planet formation in disks are constrained by the observed lifetime of circumstellar material around pre-main sequence stars. This is particularly true for the late accretion phases of giant gaseous planets.

In gas-rich disks, significant progress has been made in the past decade to find direct evidence for disk evolution. Inner holes have been found in an increasing number of proto-planetary Class II disks (e.g. LkCa15, Piétu et al. 2006), with a frequency as high as 20% (e.g. Owen & Clarke 2012). In the cavity, the evolution of the gaseous component, and how it can affect the dynamics of the small grains during the last stages of (giant) planet formation is not yet known. Near-IR images of these transitional disks revealed for instance smaller inner holes than those seen at millimeter wavelengths (Garufi et al. 2013), a possible consequence of the spatial distribution of the residual, primordial gas.

On the other hand, significant IR excess has been associated with many main sequence stars (e.g. Eiroa et al. 2013)), without any significant reservoir of gas except for a few younger (< 100 Myr) stars (Dent et al. 2013; Howard et al. 2013). In these systems, the dust lifetime is short, and therefore the observed dust must be constantly replenished from collisions between exo-asteroids and/or exo-comets. These so-called debris disks represent extra-solar analogs to our Kuiper Belt. The young β Pictoris system is an impressive example of this sub-category. It has an optically thin dust disk, and ALMA images of the cold CO emission reveal asymmetries that are attributed to the destruction of cometary-like bodies, possibly trapped by an unseen planet (Dent et al. 2014). The gas in this system is therefore not primordial.

Among young MS stars surrounded by debris disks, a handful of remarkable objects exhibit a substantial amount of primordial gas, making them hybrid disks between proto-planetary and debris disks: 49 Ceti (40 Myr, Zuckerman et al. 1995; Moór et al. 2011), HD 21997 (30 Myr, Kóspál et al. 2013), HD 141569 (5 Myr, Dent et al. 2005), and HD 131835 (16 Myr, Moór et al. 2015). This raises questions over the specific physical conditions that allow CO gas disks to survive in stars as old as 30 Myr since most disks dissipate in ∼5-10 Myr only. The dominant physical mechanisms at play that dissipate such old gas disks are photoevaporation or runaway gas accretion by unseen giant planets, which may then present different characteristics since they would accrete on a longer timescale. The paucity of such hybrid systems may be explained by the very fast dissipation of the primordial reservoir of gas, as soon as this process has started. They may represent the missing link between proto-planetary and planetary systems, as suggested by the recent analysis of the *ALMA* observations of HD 21997 by Kóspál et al. (2013), and should therefore be considered as transient systems with ongoing dissipation of their primordial gas component and last stages of (giant) planet formation. However, in some cases at least, part of

the observed CO gas may be of second generation as suggested for 49 Ceti (Roberge et al. 2013). So far, all these disks have been found around Herbig Ae stars and there are no equivalent hybrid disks observed around old T Tauri stars (Lieman-Sifry et al. 2016).

Millimeter surveys of gas in debris disks yielded low detection rates, confirming the paucity of gas-rich disks. Dent et al. (2005) reported the first detection of CO J=3→2 in 49 Ceti from *JCMT* observations out of a sample of 59 HAeBe and Vega-like stars. Pascucci et al. (2006) focused on 15 (5-100 Myr old) stars from the FEPS sample, but their *SMT* search for CO J=2→1 and J = 3→2 lines yielded only non detections and upper-limits on the gas mass. Kastner et al. (2010) also failed to detect molecular gas emission with *IRAM-30m* antenna in a sample of 10 Vega-like stars. Only recently, Moór et al. (2011) discovered a significant CO J=3→2 and CO J=2→1 emission from the 30 Myr old star HD 21997 using the *APEX*/SHFI receiver. The most sensitive survey, however, only reached upper limits on the CO gas mass of the order of $M_{\rm CO} \lesssim 0.5 - 1.10^{-3} M_{\oplus}$.

We report here a more sensitive survey of 25 debris disks in CO J=2→1 or J =3→2 using *APEX* and the *IRAM-30m* radiotelescope. With these observations, we reach a sensitivity limit similar to that of the recent work of Moór et al. (2015). We have also complemented these new observations with a compilation **of** more recent observations of dust and gas in young disks. We report the results in this paper. Section 2 outlines the sample of sources and the observations. The description of the analysis by correlation is given in Section 3 while Section 4 is an open discussion of these results.

2. Samples and data reduction

2.1. APEX and IRAM observations

We performed a ^{12}CO J = 3→2 and ^{12}CO J = 2→1 survey of the sample presented in Table 1. We selected 25 systems whose properties are similar to the recently identified gas-rich debris disks, thereby focusing on A-type stars younger than 100 Myr and with a large dust radius $R_{\rm dust}$ >30 au. The sources were collected from various *IRAS*, *Spitzer*, *WISE,* and *Herschel* debris disks studies (Rhee et al. 2007; Wyatt et al. 2007; Zuckerman & Song 2004; Patel et al. 2014; Morales et al. 2009; Chen et al. 2006; Riviere-Marichalar et al. 2014; Kennedy et al. 2014). Among the 25 selected targets, 17 are new sources for the search of CO and 8 sources had been observed in only one of these two CO transitions. We also included 2 targets with atomic gas sprectroscopic features interpreted as the signature of Falling-Evaporating Bodies (FEB) (HD 21620 and HD 42111, Welsh & Montgomery 2013).

For northern targets, we used the *IRAM-30m* telescope (project 172-14), attempting to detect the CO J=2→1 line with the EMIR receiver connected to the FTS200 backend providing 200 kHz spectral resolution. In the southern hemisphere, we used the *APEX* telescope at 345 GHz to search for the CO J=3→2 transition with the SHeFI receiver (projects 094.C-0161 and 095.C-0742).

The data reduction was done using the GILDAS/CLASS package. Spectra have been resampled to a δv=1 km.s^{-1} channel width. The baseline subtraction and rms calculation were performed on 800 channels, avoiding the contamination lines when present. The conversion from the T_A^* scale onto flux density (Jy) was done with the following factors: 41 Jy/K for *APEX* [1] at 345 GHz and 7.8 Jy/K for the *IRAM-30m* [2] at 230 GHz. The final spectra are plotted on Figs. 1 and 2, and the upper limits on CO emission are displayed as a function of the infrared excess of disks on Fig. 3. The median distance of the observed stars is 69 pc, with a standard deviation of 46 pc. Since the flux values depend on the distance of the stars, they are not directly representative of the gas mass reservoir. We therefore present the fluxes scaled at 100 pc for all 25 stars in our sample and other targets from the literature in Fig. 4.

2.2. Compilation of existing CO and mm continuum data

We have compiled measurements of the CO J=2→1 and CO J=3→2 emission from the literature, as well as the continuum emission at the corresponding wavelength for a wide variety of disks. We consider five categories: the classical T Tauri stars (CTTS), the Herbig AeBe, the weak-line T Tauri stars (WTTS), the hybrid disks, and finally the debris disks. We do not include class I objects in the sample to avoid confusion with remnant envelopes and nearby molecular clouds. The measurements are compiled in Table 2. We have retrieved the integrated emission (Jy.km.s^{-1}) for the CO lines, and the upper limits are always given at the 3σ level.

We have also included binary systems. As most of them are either spectroscopic or wide binaries, the dynamical influence on the disk should be negligible. We selected binary sources from the *ALMA* survey of Akeson & Jensen (2014). The authors focussed on the analysis of the continuum emission, and we have retrieved the CO J=3→2 emission of 15 sources from the archive (project 2011.0.00150.S). We included binaries with dynamical truncation, such as GG Tau, since no systematic effect on the ratio $S_{\rm CO}/F_{\rm cont}$ is seen. We have also used the data from the *ALMA* project 2013.1.00163.S (PI: M. Simon), which aims at determining the stellar mass of low-mass T Tauri stars by measuring the Keplerian rotation of the gas. This project adds eight sources to our compilation. In addition, for HD 21997, we have determined the upper limit on the dust emission at 1.3 mm from the archival data (project 2011.0.00780.S).

Most of these sources are in young stellar associations. The most represented complex is the Taurus-Auriga region, with approximatively half of the CTTS and Herbig AeBe, and one third of WTTS. Other stars are either isolated or belong to different clouds such as Ophiucus, upper Scorpius, TW Hya, Orion, Chameleon.

The measurements at 1.3 mm or 0.87 mm are not available for every source. However, we find a clear correlation between the observed CO J=2→1 / CO J=3→2 fluxes (scaled at 100 pc). We have thus tried to complement the missing measurements by interpolating the flux of the missing transition on this correlation line (the procedure is described in Appendix B). This assumes that the disks have physical conditions similar to those used to derive the correlation. The corresponding fluxes are represented by smaller symbols in Fig.7a and 7b.

3. Results and analysis

3.1. Outcome of the APEX and IRAM survey

Our *IRAM* and *APEX* surveys were designed to provide a homogeneous sensitivity for the whole sample, and to reach a high-enough sensitivity on the integrated intensity to detect dim systems such as 49 Ceti at a > 5σ level. This corresponds, for a

[1] http://www.apex-telescope.org/telescope/efficiency/

[2] http://www.iram.es/IRAMES/mainWiki/Iram30mEfficiencies/

Table 1: **Observational parameters for our sample of debris disks.**

Name	LSR velocity ($km.s^{-1}$)	$L_{IR}/L_\star$	Ref	$3\sigma_{int}$ ($Jy.km.s^{-1}$)	M_{H_2} DiskFit (3σ upp. limit) $M_\oplus$	M_{H_2} from S_{CO} (3σ upp. limit) $M_\oplus$
IRAM-30m - CO J=2→1						
HD 2772	-5.4	8.2×10^{-6}	1	<0.569	< 0.110	< 0.454
HD 14055	7.5	6.7×10^{-5}	1	<0.387	< 0.008	< 0.027
HD 15115	-0.2	4.8×10^{-4}	2	<1.89	< 0.063	< 0.229
HD 21620	-22.8	2.51×10^{-5}	3	<0.622	< 0.383	< 0.819
HD 23642	-4.0	2.2×10^{-5}	1	0.71 ± 0.18	0.18 ± 0.04	0.57 ± 0.14
HD 31295	-3.5	4.7×10^{-5}	1	<0.768	< 0.016	< 0.058
HD 42111	8.4	1.00×10^{-5}	3	<0.902	< 1.02	< 2.16
HD 159082	7.1	5.7×10^{-5}	1	<0.497	< 0.132	< 0.537
HD 218396	-12.6	2.29×10^{-4}	4	<0.349	< 0.005	< 0.032
APEX - CO J=3→2						
HD 225200	13.4	7.4×10^{-5}	1	<3.15	< 0.260	< 0.470
HD 17848	16.7	4.8×10^{-5}	1	<10.5	< 0.146	< 0.242
HD 24966	11.7	3.1×10^{-4}	1	<2.85	< 0.166	< 0.278
HD 30422	-4.8	3.7×10^{-5}	1	<2.22	< 0.036	< 0.063
HD 35850	1.4	2.3×10^{-5}	1	<2.26	< 0.007	< 0.015
HD 38206	5.8	1.4×10^{-4}	1	<2.78	< 0.062	< 0.119
HD 54341	20.0*	1.9×10^{-4}	1	<2.49	< 0.106	< 0.232
HD 71043	5.9	6.5×10^{-5}	1	<2.74	< 0.073	< 0.131
HD 71155	-4.7	4.2×10^{-5}	1	<2.66	< 0.017	< 0.035
HD 78072	2.5	2.5×10^{-4}	1	<2.11	< 0.071	< 0.133
HD 136246	4.2	4.9×10^{-5}	1	<2.47	< 0.281	< 0.459
HD 164249	2.5	7.2×10^{-4}	1	<2.38	< 0.020	< 0.049
HD 166191	3.8	1.0×10^{-1}	5	<2.77	< 0.187	< 0.351
HD 181296	14.3	2.4×10^{-4}	1	<2.19	< 0.014	< 0.046
HD 182681	10.5	1.95×10^{-4}	4	<2.91	< 0.083	< 0.124
HD 220825	-1.5	2.9×10^{-5}	1	<2.29	< 0.011	< 0.046

Notes. * The radial velocity of HD 54341 was kindly provided by F. Kiefer, see Kiefer (2016). Stars in italics are systems with earlier detection limits in one CO transition, see §2.1. References for $L_{IR}/L_\star$: 1 - Chen et al. (2014); 2 - Moór et al. (2011); 3 - Roberge & Weinberger (2008); 4 - Rhee et al. (2007); 5 - Schneider et al. (2013). The last three colums show the 3σ upper limits derived from our study: on the integrated intensity of CO, the H_2 mass derived from DiskFit model and the H_2 mass directly derived from the integrated flux. The integrated flux and the H_2 masses for the tentative detection around HD 23642 are also displayed.

channel width of 1 $km.s^{-1}$, to a 6 mK rms value for T_A^* with *APEX* and 6.5 mK with the *IRAM-30m* telescope. Most targets present no CO line detection, and we report the $3\sigma_{int}$ upper limits on the integrated intensity, with the standard formula $\sigma_{\rm int} = \sigma.\sqrt{\Delta v \delta v}$, σ being the intensity rms in a single channel. Although typical line widths of approximately 5 $km.s^{-1}$ are observed around A-stars with detected CO lines, we assume here δv = 10 $km.s^{-1}$ for the sake of comparison with previous studies. Contamination from the cloud environment is seen for five sources: HD 218396, HD 42111, HD 21620, HD 166191, and HD 136246. For each CO transition, we also stacked the spectra of all observed targets, after correcting for the known system velocities, in order to improve the global signal-to-noise ratio, but this did not yield any tentative detection. The stacked spectra are displayed in green in the last insets of Fig. 1 and 2. In Table 1, we present the flux density upper limits for seven new targets in the CO J=2→1 transition, and two stars that had already been targeted in the CO J=3→2 transition (namely, HD 15115 and HD 218396). The median value is 0.8 Jy $km.s^{-1}$ ($3\,\sigma_{\rm int}$). With *APEX*, we report upper limits for ten new targets and improve the detection limits by a factor two at least for the other disks (median value $3\sigma_{\rm int}$ = 2.6 Jy $km.s^{-1}$), compared to earlier studies Kastner et al. (2010), Moór et al. (2011), Hales et al. (2014), except for HD 17848 where Moór et al. (2015) obtained more sensitive data.

3.2. A possible new hybrid disk candidate in the Pleiades

We report a tentative detection of CO J=2→1 for the double-lined eclipsing binary HD23642 (A0Vp(Si)+Am, P = 2.46 d, Abt & Levato 1978; Torres 2003; Munari et al. 2004). The system is classified as a debris disk with a weak infrared excess detected by *Spitzer* (Su et al. 2006; Morales et al. 2009; Chen et al. 2014). The peak emission is found around 24 μm, although there is only an upper limit on the flux at 70 μm. Here we adopt the fractional excess luminosity reported by (Morales et al. 2009), $L_{IR}/L_\star = 1.7\times10^{-5}$, which relies on the shape of the IRS spectrum in the 20-33 μm range. The binary is composed of two A-type stars, located in the Pleiades group. Its distance has been revised to 138 ± 1.5 pc by Groenewegen et al. (2007), in agreement with the recent works on the distance of the Pleiades.

The spectrum (see Fig.5) presents a double-peaked line, with an intensity integrated over the channels -8 to +2 $km.s^{-1}$ estimated to 710 ± 180 mJy km s^{-1}. The line center is at ∼ −4 $km.s^{-1}$, consistent with the binary radial velocity of $V_{\rm LSR}$ = −3.6 ± 0.1 $km.s^{-1}$ determined by Groenewegen et al. (2007). This signal is unlikely to be due to contamination by a molecu-

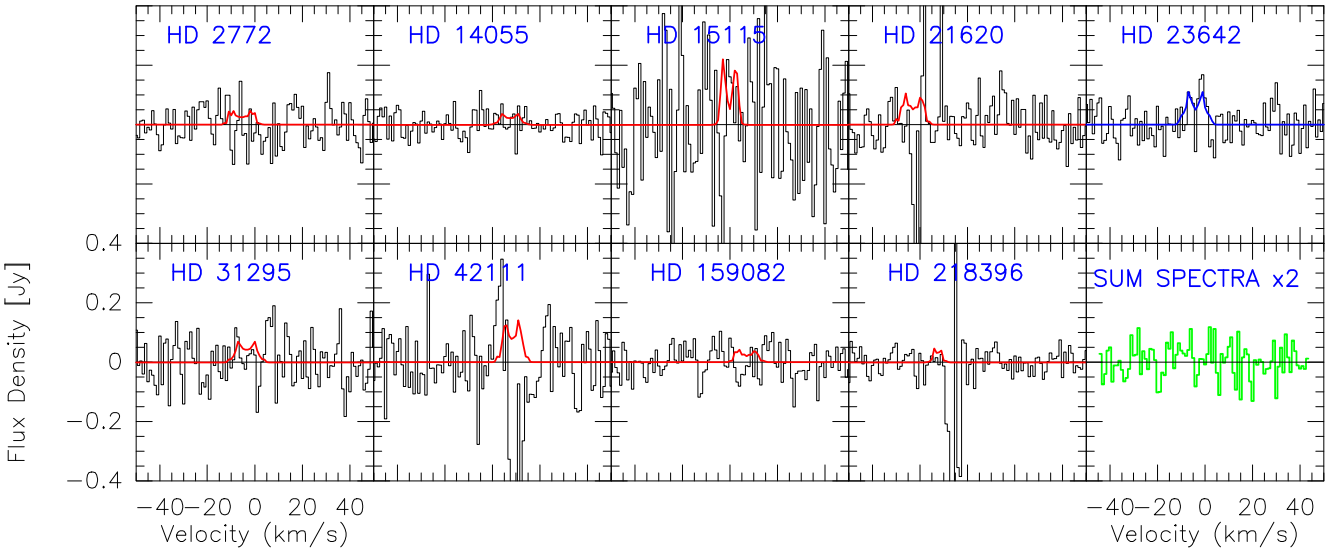

Fig. 1: CO J=2→1 spectra obtained with the *IRAM-30m* telescope. Fluxes are in Jy with respect to local standard of rest (LSR) velocity. The last box shows the cumulated spectrum made with spectra shifted in velocity to set the systemic velocity to zero (note that the flux scale is different from the individual spectra). The sources with a high rms or showing strong contamination (i.e., HD 15115, HD 21620, HD 42111 and HD 218396) are not used to produce the cumulated spectrum. The 3σ upper limit model for each spectrum is over-plotted in red (see sect. 3.3) except for the HD 23642 spectrum, where the best-fit model for the tentative detection is plotted in blue.

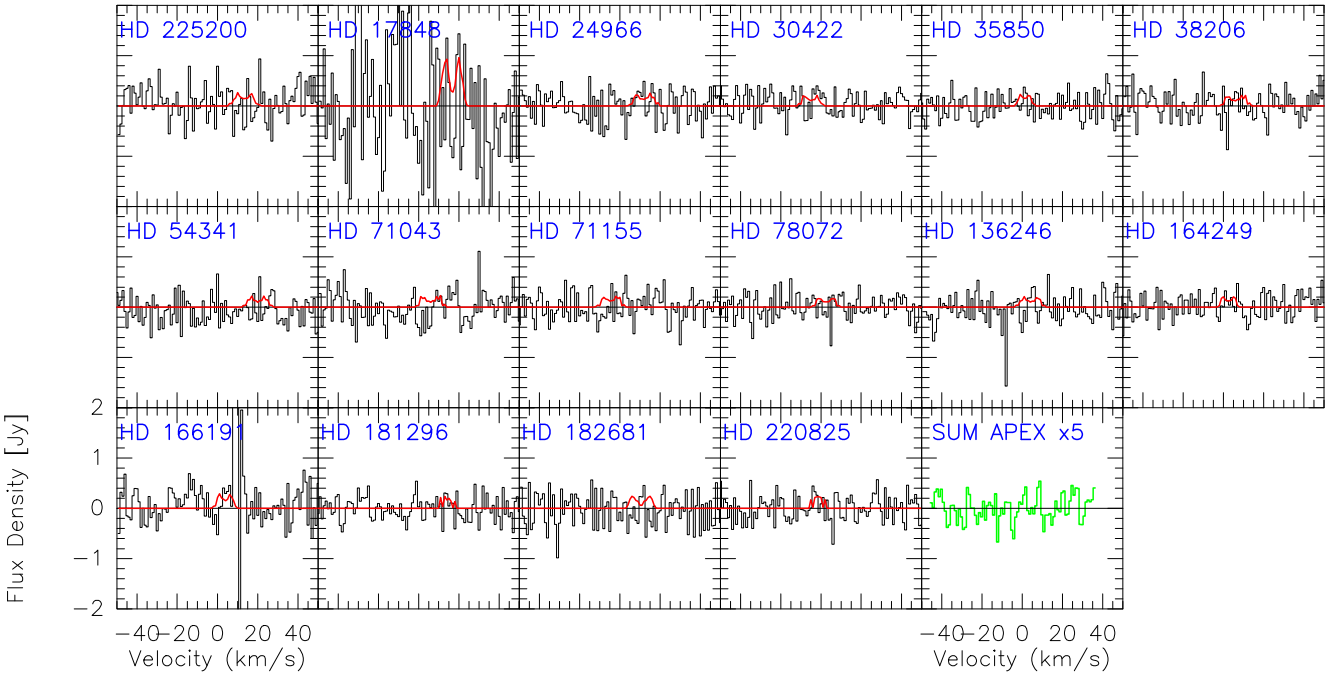

Fig. 2: CO J=3→2 spectra obtained with the *APEX* telescope. Fluxes are in Jy with respect to LSR velocity. The last box shows the cumulated spectrum made with spectra shifted in velocity to set the systemic velocity to zero (multiplied by factor five). The sources with a high rms or showing strong contamination (i.e., HD 17848 and HD 166191) are not used to produce the cumulated spectrum. The 3σ upper limit model for each spectrum is over-plotted in red (see sect. 3.3).

lar cloud emission: although CO emission is present towards the Pleiades region, it appears at LSR velocities of ~7 and 10 km.s^{-1} (Breger 1987; White 2003).

If we interpret this signal as emission from a Keplerian disk, given the total stellar mass derived from spectroscopic data (2.23 $M_\odot$ and 1.57 $M_\odot$), and the inclination set to 78° (e.g., Groenewegen et al. 2007), the separation of the two peaks in the CO line suggests a disk outer radius much larger than 200 au. Using the DiskFit tool (see Sect.3.3), the best-fit model yields R_{out} = 450 ± 210 au, and a CO gas column density at 100 au of $\Sigma_0 = 6.0 \times 10^{14} \pm 1.3 \times 10^{14}$ cm^{-2} (4.6σ detection). The best fit model is overplotted in Fig. 5.

The derived mass of gas in this system would be similar to that of the 20-40 Myr old systems HD 21997 and 49 Ceti, for which the gas origin is debated. Given the estimated age of the Pleiades cluster (~125-130 Myr, Stauffer et al. 1998; Castellani

et al. 2002), the presence of such a large amount of remnant gas is puzzling and makes it the oldest hybrid disk candidate. Further observations are necessary to definitely confirm our finding, however the double-peaked line shape centered at the expected stellar velocity suggests a robust detection.

3.3. CO mass upper limits

The upper limits on CO integrated emission can be translated into limits on the remnant mass of H_2 gas. We derive the gas mass using two methods. The first is based on the rms obtained from the data. The second properly takes into account the velocity gradient resulting from Keplerian shear by using a disk model. Conversion to H_2 content is done using the standard value of 10^{-4} for the CO to H_2 abundance ratio.

Gas mass inferred from the rms of the flux density: Here we follow the approach used by many authors and derive the CO content assuming T_{ex} = 40 K for the excitation temperature and τ = 1 for the opacity (see Appendix A.1). These values allow a direct comparison with the literature (although a temperature T_{ex} = 20 K is sometimes assumed). Results are shown in Table 1. Some sources have been observed in CO J=2→1 and 3→2. The flux ratio and H_2 masses derived from the two transitions are shown in Table B.1. The discrepancy in derived masses illustrates the limits of our assumptions. We note also that Kóspál et al. (2013) have derived excitation temperatures lower than 9 K for the ^{12}CO in the HD 21997 disk.

Fig. 6 displays the total gas mass (H_2) consistently derived using this method as a function of the dust fractional luminosity, for sources from past surveys and from this work (larger symbols). The median value for the limits on the gas mass (M_{H_2}) in our sample is 0.1 $M_\oplus$ (3σ). The tightest constraint is obtained for HD 14055 in CO J=2→1 and HD 35850 in CO J=3→2 transition with a limit as low as $\sim$0.03 $M_\oplus$, that is, 2 $M_{\rm Moon}$ of H_2, a value equivalent to (even slightly less than) the amount of gas recently detected with *ALMA* in the young β Pic system by Dent et al. (2014).

Gas mass inferred from a Keplerian disk model: The gas mass can also be estimated by constraining the surface density in a disk modeling approach, as done in Dutrey et al. (2011) and Chapillon et al. (2012). For this purpose, we used the DiskFit code (Piétu et al. 2007), dedicated to the simulation of Keplerian disks. We describe the radial physical properties of disks as power-laws, in a similar analysis to resolved disks. The disks are assumed to be in Keplerian rotation around their central stars, the mass of stars being estimated from their stellar types. [3] We assume for the disk model an outer radius R_{out} = 200 au, a typical value for the resolved hybrid disks, and an inner radius R_{in} = 5 au. For six disks, the inclination is known from resolved scattered light observations: 80° for HD 182681, 73° for HD 17848 (Moór et al. 2015), 56.7° for HD 71155 (Booth et al. 2013), 86° for HD 15115 (Mazoyer et al. 2014), 26° for HD 218396 (Matthews et al. 2014). For HD 181296, we have set the inclination to the 20° upper limit determined by Smith et al. (2009). The most probable value of 60° is assumed for the other disks. The temperature law is set to 30 K at 100 au with the exponent of the radial variation q = 0.4. With an assumed exponent of p = 1.5 for the surface density (see Piétu et al. 2007, for case studies), the surface density at 100 au Σ_0 is the only free parameter.

The model spectra corresponding to the 3σ upper limits on Σ_0 are superimposed in red to the spectra in Fig.1 and 2. In addition, the best fit model for the tentative detection in HD 23643 is displayed in blue. The corresponding 3 σ upper limits on the total disk masses are reported in Table 1 (see Appendix A.2 for details). The derived gas masses are a factor of two or three lower than from the simple uniform $T_{\rm ex}$ approach (see Table 1), as a result of different assumptions. As it accounts for density and temperature gradients, the method using DiskFit should be considered as more reliable.

3.4. Detection statistics

Our survey adds 17 new systems to the sample of young debris disks which have been searched for molecular gas. Taking into account these new constraints in addition to the surveys of Kastner et al. (2010), Moór et al. (2011), Hales et al. (2014), the recent survey of Moór et al. (2015) with the discovery of HD131835, and the *ALMA* detections of gas around HIP 84881 and HIP 76310 in the survey of Lieman-Sifry et al. (2016), we can derive an approximate estimate of the occurrence of CO gas in young debris disks: 7.1 ± 2.6 % (1σ uncertainty, 7 detections among 98 observed systems). This value can be considered as a lower limit since only less than half of the targets have been observed with enough sensitivity to detect a CO luminosity as large as that of HD 21997/49 Ceti (see Fig. 4). The occurrence of a CO gas disk as bright as HD 21997/49 Ceti (after scaling at 100 pc) is 12.2 ± 4.7% (1σ) (6/49 detections).

This value suggests that such systems are very rare, likely because they represent a very short transient phase in the evolution of circumstellar disks. It should also be recognised that this detection frequency does not rely on a homogeneous sample: the observed targets are located in different regions of the sky, may span a broad range of ages, and the various surveys have reached different sensitivity limits. The occurrence of hybrid disks (with secondary dust and possible primordial CO gas) is even smaller, since the origin of the detected CO gas is still debated for most gas-rich debris disks (HD 141569, HD 21997, 49 Ceti and HD 131835). Several authors favor a secondary origin (Moór et al. 2011; Zuckerman & Song 2012) for some of these systems, as is the case for the famous β Pictoris disk, where the CO gas detected by *ALMA* may have been produced by a massive collision of planetesimals (Dent et al. 2014). Besides β Pic, the detected systems with the weaker CO emission (or gas mass) are HD 21997 and 49 Ceti (see Fig. 4 and 6). These two are therefore the most probable candidates for a secondary origin of the gas, although the gas mass remains one order of magnitude larger than in β Pic.

Among the stars in our study, we note that 17 disks (45 when including the surveys from the literature), that is, 68% of our sample (resp. 48%), are constrained to CO gas masses smaller than that of 49 Ceti, and one of them, HD 35850, shows even less CO gas than β Pictoris.

3.5. CO to dust flux ratio correlations

To better understand the peculiarity of hybrid disks, we compare their properties with those of other (proto-planetary) disks. For this purpose, we have chosen to study the ratio of the emission of CO over the emission of the dust, $\frac{S_{\rm CO}}{F_{\rm cont}}$. In the literature, we find many studies considering the ratio of masses, but the mass is

[3] http://www.uni.edu/morgans/astro/course/Notes/section2/spectralmasses.html

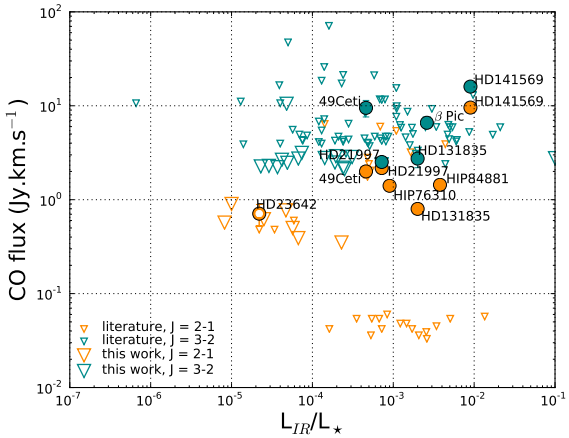

Fig. 3: CO line flux as a function of infrared excess. Circles indicate CO detection, and triangles indicate upper limits. Large symbols are from our survey, and small symbols for literature data (Dent et al. 2005; Kastner et al. 2010; Moór et al. 2011, 2015; Hales et al. 2014; Lieman-Sifry et al. 2016)). Orange symbols stand for the CO J=2→1 measurements and green symbols for CO J=3→2 measurements. The tentative detection around HD 23642 is plotted with an empty circle.

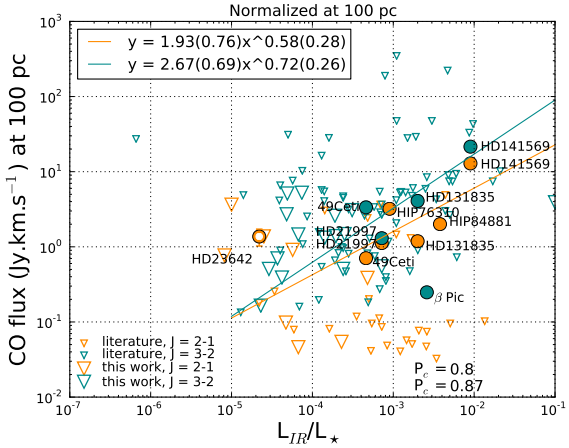

Fig. 4: Integrated flux of CO normalized at 100 pc compared to the infrared fractional luminosity of the debris disks. The same disks and symbol/color code are used as in Fig. 3.

always a calculated value, depending on models and on assumptions about excitation conditions and dust-to-mass ratio, etc. On the contrary, the $\frac{S_{CO}}{F_{cont}}$, which is an equivalent width, is a distance-independent product of observations that is not affected by hidden assumptions or biased by interpretation models. It may be impacted by the diversity of optical depths in the disks, but we show in the following that this ratio presents some characteristic trends that can be explained easily when considering the possible opacity conditions.

The diagrams on Fig. 7a and 7b summarize the results displayed in Table 2 by plotting the CO integrated emission as a function of the dust emission at the corresponding wavelength, and scaled at 100 pc. As some data have no given error bars, or very small ones, we have added a 10 % error bar on the whole sample in order to homogenize the sample and better account for calibration uncertainties. Different colors are used

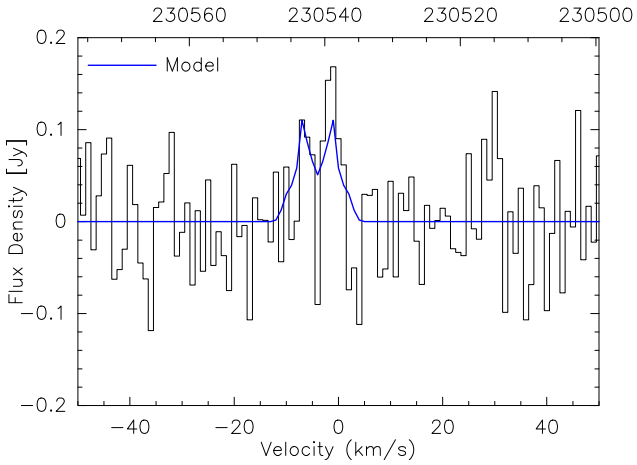

Fig. 5: CO J=2→1 spectrum of HD 23642 obtained with the *IRAM-30m* telescope. Flux is in Jy with respect to LSR velocity. A line is detected at the 4σ level, at the star velocity (-3.6 km.s^{-1}). The model of the line is displayed in blue.

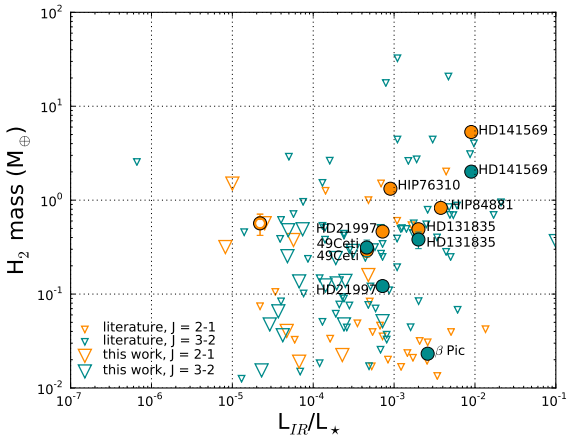

Fig. 6: Mass of H_2 (from Scoville et al. (1986)) compared to the infrared fractional luminosity of the debris disks. The same disks and symbol/color code are used as in Fig. 3.

to represent the five categories of disks: blue indicates the CTTS, violet the Herbig AeBe disks, orange the WTTS, red the hybrid disks and green the debris disks. Only 13 sources are common to both diagrams. As for the transitional disks, we do not distinguish them from the CTTS category as their position on the diagrams does not depart from the CTTS group. For the CO J=2→1 / 1.3 mm emission, we have considered 33 sources where both gas and dust are detected. Among them, six sources are displayed with a lower limit arrow, meaning that the CO emission might be contaminated by the environment. 6 sources have only an upper limit on the gas emission, 3 on the dust emission (one having a lower limit on the gas), and 20 sources have upper limits both on the gas and the dust emission (mostly WTTS from Hardy et al. (2015)). For the CO J=3→2 / 0.8 mm emission, 42 sources have the continuum and gas emission detected, 3 have only upper limits on the gas emission and 1 has upper limits on the gas and dust emissions.

There is a clear correlation between the emission of the gas and that of dust at mm wavelengths, with naturally decreasing

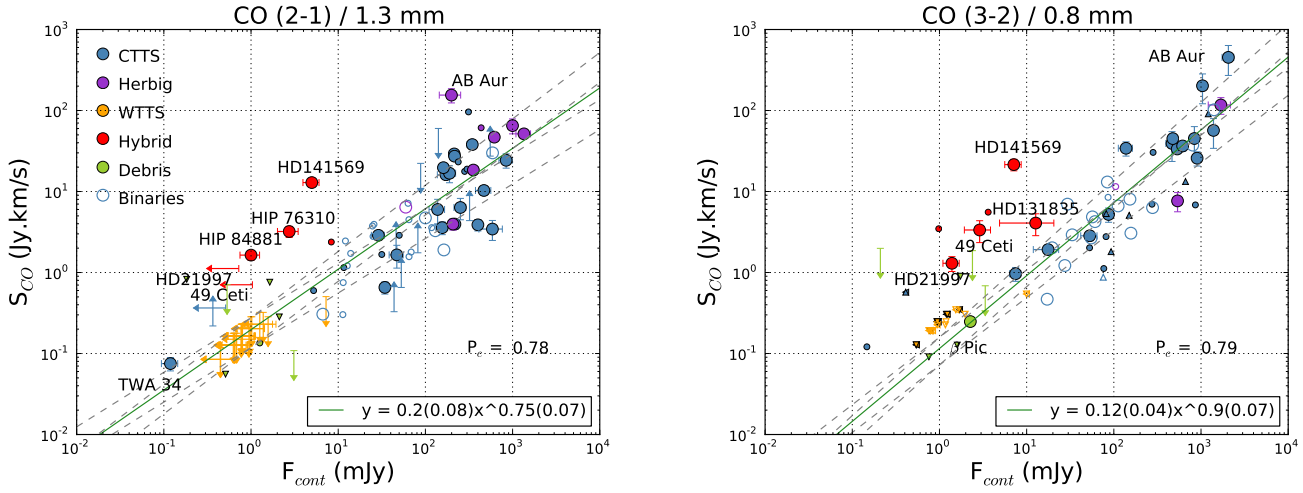

Fig. 7: (a) CO J=2→1 emission plotted with the corresponding continuum measurement, the fluxes being normalized at 100 pc. Blue corresponds to CTTS, violet to Herbig, orange to WTTS, red to hybrid and green to debris disks. The open circles mark the binary systems. The Pearson coefficient of correlation of the data, P_c, is indicated in the lower right-hand corner.
(b) As for Fig. 7a but for the CO J=3→2 / 0.8 mm emission.

flux densities for more evolved systems, such as in WTTS or debris disks. The correlation is seen both at 1.3 mm and 0.8 mm.

The sample spans at least three orders of magnitude in flux density and we observe an almost linear correlation between dust and gas emissions on Fig. 7a and 7b, with no clear evidence for a slope break (although there are many more sources in the upper right-hand corner of the diagram than in the faint dust/CO emission region where the optically thin regime is expected to be found). There is no obvious difference between CTTS, HAeBe, single, and wide binary stars. A few sources lie well above the global trend: most of them are suspected hybrid disks (HIP 84881, 49 Ceti, HD 21997 and the most prominent outlier HD 141569) with the exception of the Herbig Ae (envelope embedded) star AB Aur. The dispersion around the best-fit line is less than one order of magnitude. The absence of a break in the correlation suggests that the majority of the detected gas disks might still be in the optically thick regime, while optically thin gaseous disks (expected at the last stages of the protoplanetary disk dispersal or in young debris disks) remain mostly undetected so far.

Finally, we notice on Fig.4 that there could also be a correlation between the CO integrated flux (scaled at 100 pc) and the dust fractional luminosity for hybrid disks. However, this trend is based on very few detected gas-rich debris disks so far, and their fractional luminosity spans over approximately one decade only. If it were confirmed, this trend combined with the sensitivity limits of current surveys (at the level of 49 Ceti emission) could partly explain the very low occurrence of CO detections in disks with weak IR excess ($L_{IR}/L_\star < 5.10^{-4}$). We note that the new candidate HD 23642 does not fit well on that possible trend, although its IR excess is still poorly constrained at far-IR wavelengths. The binary nature of the source (with a larger stellar mass and a suggested larger disk than other hybrid disks) may also be responsible for the discrepancies.

3.6. Search for correlations between the CO/dust flux ratio and the stellar parameters

The equivalent width, that is, the ratio $S_{\rm CO}/F_{\rm cont}$, has been calculated for the whole sample of 103 sources. We obtain an estimate of $S_{\rm CO}/F_{\rm cont}$ for 73 different sources; 46 at 1.3 mm and 44 at 0.8 mm. The ratio was not calculated when only upper limits exist for both the gas and the continuum. For some sources, the flux was interpolated at 1.3 or 0.8 mm based on the observed correlations (see Appendix B). The ratio $S_{\rm CO}/F_{\rm cont}$ was then plotted against the spectral type (Fig. 8), the stellar mass (Fig. 9), the stellar luminosity (Fig. 10), the accretion rate (Fig. 11), and the age (Fig. 12) of the stars when they are known. We have retrieved the spectral type for 98 sources, the stellar mass for 85 sources and the stellar luminosity for 71 sources.

In the figures, the median value, the first and third quartiles, Q1 and Q3 (respectively delimiting values below which 25% and 75% of the sources lie), and the 5th and 95th percentiles, P5 and P95 (respectively delimiting values below which 5% and 95% of the sources lie) are drawn for a better understanding. The name of the sources is specified only for values out of P5 and P95.

Spectral type, $M_\star$ and $L_\star$: There is no correlation between the ratio $S_{\rm CO}/F_{\rm cont}$ and either the spectral type (Fig. 8), stellar mass (Fig.9), or stellar luminosity (Fig.10). However, A stars (heavier than 2 $M_\odot$) tend to have a higher $S_{\rm CO}/F_{\rm cont}$ ratio. This trend is mainly dominated by the hybrid disks, where the ratio is approximately 1000 km.s^{-1}, compared to the median value ~100 km.s^{-1}. Among the Herbig AeBe, only AB Aur shows a high ratio, most likely because of the presence of its envelope (see §3.7.1).

Accretion rate: We have found in the literature the accretion rates for 40 sources. We do not observe any correlation in the corresponding diagram (Fig. 11). We do not observe any correlations in the diagrams. This may partly reflect the lack of data (only 39% of the sources have measured accretion rates), in particular for the older population (hybrids and debris). At

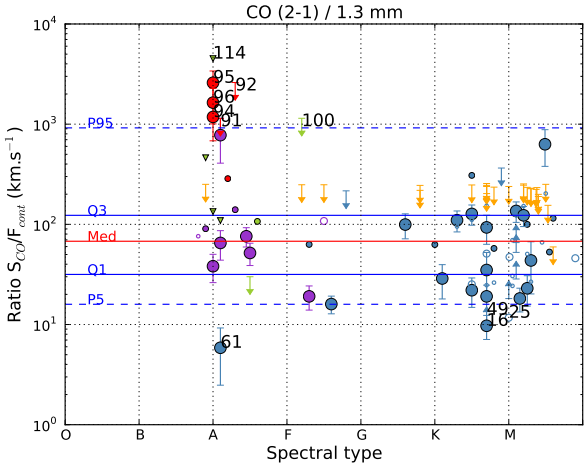

Fig. 8: Ratio S_{CO}/F_{cont} plotted against the spectral type of the stars, at 1.3 mm. The color code is the same as in Fig. 7a and 7b: blue for CTTS, violet for Herbig, orange for WTTS, red for hybrid and green for debris disks. Some statistics are represented by the horizontal lines: the red full line shows the median value of the ratio for the distribution of points, the blue full lines represent the first and third quartiles (50% of the points are between these two lines) and the blue dashed lines show the 5th and 95th percentiles (90% of the points between the lines).

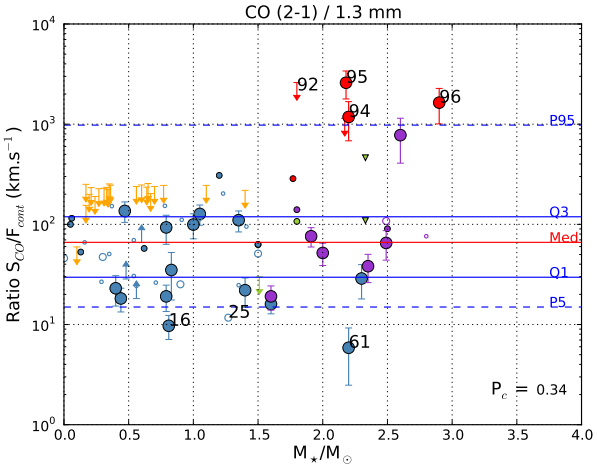

Fig. 9: Ratio S_{CO}/F_{cont} at 1.3 mm plotted against the stellar mass. The color code and lines are the same as in Fig. 8. The Pearson coefficient of correlation of the data, P_c, is indicated in the lower right-hand corner.

mm wavelengths, the emission is mostly dominated by the outer parts of the disks, and the sensitivity on inner parts is limited. Since the accretion tracers reflect phenomena occuring close to the star, it is not surprising that the global emission of the disk is not correlated to the the local inner accretion signatures. Measurements or at least upper limits on the accretion rates on more evolved stars might help, but it seems that accretion signatures are not a good tracer for evaluating the global evolution of the material around disks.

Age: We have retrieved the age of 82 sources and present the relationship between the ratio S_{CO}/F_{cont} and age in Fig. 12. A trend is observed for older disks to have higher S_{CO}/F_{cont} ratios. Nevertheless, as already noted in paragraph 3.6, the trend is mainly driven by the hybrid disks, and possibly affected by the difficult determination of ages of young stars.

3.7. Outliers

Here we list the disks that seem to have an equivalent width S_{CO}/F_{cont} departing from the observed median value 100 km.s^{-1}, that is, lying below the 5th quartile and above the 95th quartile in the different diagrams presented in section 3.6. With the exception of AB Aur, all sources having a high flux ratio belong to the category of hybrid disks.

3.7.1. Objects with high equivalent width

HD 141569 The star of spectral type B9.5V/A0Ve is located 116 pc and has two M-star companions that may be unbound (Reche et al. 2009). The age of the triple system is approximately 5 ± 3 Myr (Weinberger et al. 2000; Merín et al. 2004). With a stellar mass of 2$M_\odot$, the HD 141569A star+disk system appears in an intermediate evolutionary stage compared to the

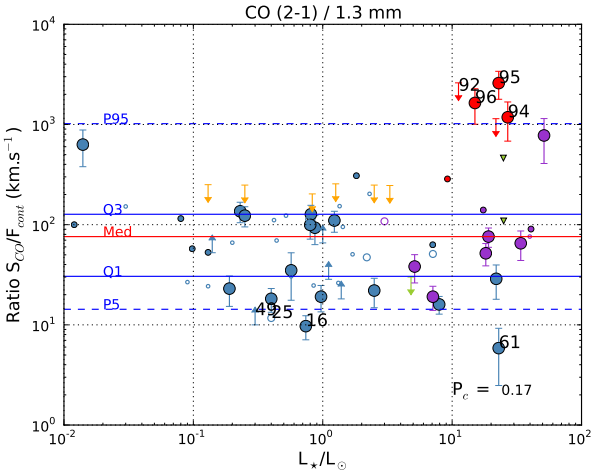

Fig. 10: As Fig. 9 but as a function of stellar luminosity.

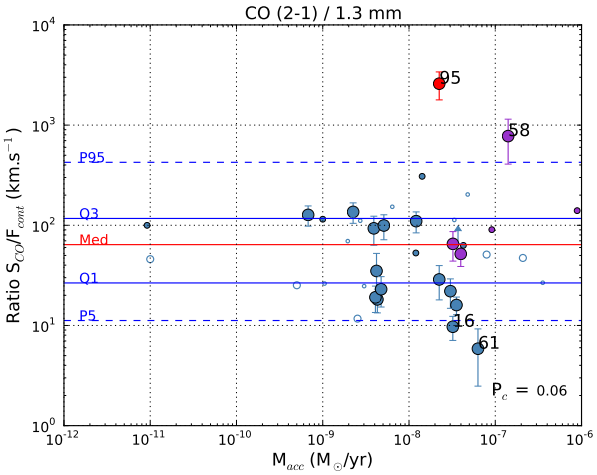

Fig. 11: As Fig. 9 but as a function of accretion rate.

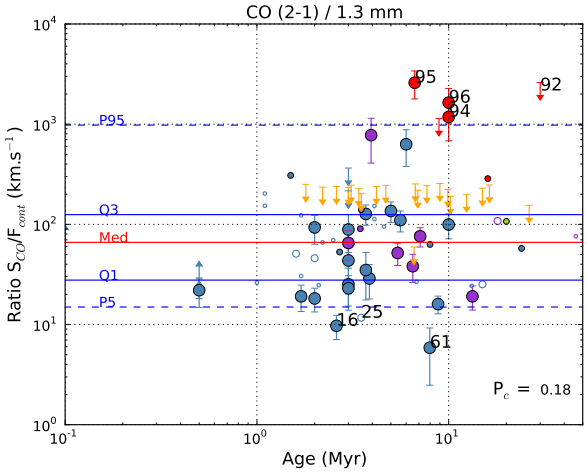

Fig. 12: As Fig. 9 but as a function of system age.

younger gas-rich system AB Aurigae (Piétu et al. 2005; Tang et al. 2012) and the more evolved β Pictoris disk. The debris disk of HD 141569 (Meeus et al. 2012, $L_{IR}/L_\star = 9\times10^{-3}$), presents a complex multiple-ring architecture with spirals and gaps imaged in scattered light by the HST (Augereau et al. 1999; Weinberger et al. 1999; Mouillet et al. 2001; Boccaletti et al. 2003; Clampin et al. 2003). A large quantity of molecular and atomic gas is still present (Zuckerman et al. 1995; Brittain et al. 2003; Dent et al. 2005; Goto et al. 2006; Brittain et al. 2007; Salyk et al. 2011; Thi et al. 2014). The CO gas extends out to ~250 au (Flaherty et al. 2016; Pericaud et al. 2016).

HD 21997 A gaseous disk around HD 21997 discovered by Moór et al. (2011) in a survey of gas around young debris disks ($L_{IR}/L_\star = 7.2\times10^{-4}$, Chen et al. (2014)). Located at 72 pc, the A3 star is a member of the Columba association, which is estimated to be ~ 30 Myr old (Moór et al. 2006; Torres et al. 2008). Given the age of the star and the amount of CO, Zuckerman & Song (2012) have proposed that the gas could be produced by collisions of comets. Nevertheless, the detailed study of the system with *ALMA* resolved observations (Moór et al. 2013; Kóspál et al. 2013) reveals that the gas and the dust are not co-located, which could imply that they have a different origin: the gas might still be primordial while the dust is of second generation.

49 Ceti The system is very similar to HD 21997: the spectral type of this 59 pc distant star is A1, and it is associated with the 40 Myr Argus group (Zuckerman & Song 2012; Torres et al. 2008). It is one of the first debris disks ($L_{IR}/L_\star = 4.6\times10^{-4}$, Chen et al. (2014)) where CO gas was detected (Zuckerman et al. 1995). The origin of the gas is still debated, and the comparison of the resolved *ALMA* observations of the dust with the gas (Hughes et al. 2008) will help to decipher its origin, currently proposed to be either primordial or secondary.

HD 131835 The gas disk around HD 131835 was discovered using the same approach as for HD 21997, during a survey to detect gas in debris disks (Moór et al. 2015). They have detected the J = 3→2 transition at a 5σ level, but no significant emission is observed for the CO J=2→1 and CO J = 4→3. In addition to the gas detection, they have deeply studied the disk thanks to the *Herschel*, *Spitzer,* and *FEROS* instruments. The dust is resolved at 70 and 100 μm, extending, on average, to 170 au, with a fractional dust luminosity $L_{IR}/L_\star$ of 2.0×10^{-3} (Chen et al. 2014). This A2-type star (122 pc) is young (16 Myr, Pecaut et al. (2012)), and thus represents another example of a gas-rich debris disk, possibly of the hybrid kind: the analysis of the gas by Moór et al. (2015) does not rule out a primordial origin.

HIP 84881 The disk of HIP 84881 has been revealed by the analysis of *WISE* photometric data (Rizzuto et al. 2012). Its infrared fractional luminosity is of the same order of magnitude as HD 141569, HD 131835, and β Pic ($f = 3.78^{-3}$, McDonald et al. (2012)). This has motivated the search for gas in this young debris disk with *ALMA*. Both the CO and continuum are detected at 1.3 mm (Lieman-Sifry et al. 2016). The dust disk has a marginally resolved inner radius, <20 au and extends out to 150 ±30 au.

HIP 76310 In addition to HIP 84881, HIP 76310 is the other new hybrid disk discovered by Lieman-Sifry et al. (2016). The infrared excess has been detected by *Spitzer* (Carpenter et al. 2006), and is the strongest excess among A-B stars in Upper Sco ($L_{IR}/L_\star = 9\times10^{-4}$ after Chen et al. (2014)). The millimeter emission at 1.2 mm was detected first by Mathews et al. (2012) with the IRAM 30 m, and recently by *ALMA*, as well as ^{12}CO J=2→1 emission (Lieman-Sifry et al. 2016). The dusty disk has a resolved inner cavity of ~70 au.

AB Aurigae This is a younger Herbig Ae system of the Taurus region, ~4 Myr old. The A1-type star is surrounded by a large flared disk of gas and dust. A 100 au inner depletion of material is observed (Piétu et al. 2005), as well as spirals both in the gas and dust warped distributions (Fukagawa et al. 2004; Hashimoto et al. 2011; Tang et al. 2012). A large envelope remains present around the system (r~1300 au, Grady et al. (1999)), from which material could be accreted despite its evolved age (Tang et al. 2012). Consequently, the high ratio of CO emission compared to the dust might be affected by this remnant envelope.

3.7.2. Objects with low equivalent width

HD 245185 This A type star HD 245185 is part or the λ Orionis cloud, located 450 pc away, even if the membership of the Taurus region is not excluded (Ansdell et al. 2015). Several studies have demonstrated that the star is accreting material from a primordial disk (Finkenzeller & Mundt 1984; Herbst & Shevchenko 1999; de Winter et al. 2001; Hernández et al. 2004; Acke et al. 2005; Wade et al. 2007; Hernández et al. 2010; Donehew & Brittain 2011). Ansdell et al. (2015) have observed the detected CO J=2→1 emission and the dust at 850 μm. They observe a mid-IR dip in its spectral energy distribution (SED), which could be the sign of a gap in the disk.

DL Tau A dust disk around DL Tau was first detected by Beckwith et al. (1990), followed by the observation of CO gas (Koerner & Sargent 1995; Simon et al. 2000), CN (Guilloteau et al. 2014), and H_2CO (Guilloteau et al. 2013), despite strong confusion. While the CO and CN extends out to ~460 au, the dust disk is smaller, with an outer radius of 150-180 au (Guilloteau et al. 2011; Kwon et al. 2015). Contamination by the molecular cloud may have affected the integrated line flux.

DQ Tau This is a spectroscopic binary, part of the Taurus-Auriga complex, implying a distance of ~140 pc and a young age (1-3 Myr). With an orbital period of 15.8 days, the stellar separation is ~0.1 au (Mathieu et al. 1997). The authors deduce that the disk truncation effect by the binary is limited to the inner 0.4 au region, and that no effect is visible on the SED compared to a single classical T Tauri disk. Warm CO and dust have been detected in this region (R_{CO} ~0.1 au, Carr et al. (2001), R_{dust} ~0.2 au, Boden et al. (2009)). The system is strongly accreting material from the circumbinary disk, as attested by the variability of the infrared and radio emissions (Salter et al. 2008; Bary & Petersen 2014). The gas emission is faint, and only ^{12}CO has been detected (CN and H_2CO search led to non-detections, strong ^{13}CO confusion, Guilloteau et al. (2013)). Williams & Best (2014) estimate the gas disk mass to be lower than 10^{-3} $M_\odot$ and the dust mass lower than 9×10^{-5} $M_\odot$.

BP Tau Like DQ Tau, BP Tau is a member of the Taurus cloud, but is a single star harboring a CO disk extending out to 120 au, and a dust disk larger than 100 au (Dutrey et al. 2003). This makes BP Tau one of the most compact disks detected. Dutrey et al. (2003) argue that the ^{12}CO is optically thin, which could explain its low position on the diagram.

4. Discussion

4.1. Interpretation of the S_{CO}/F_{cont} correlations

Fig. 7a and 7b reveal an interesting correlation that can be interpreted as follows: different regimes of opacity correspond to different regions of the diagrams. Depending on the dust/gas opacity, the emission is governed by different disk physical parameters. Following the standard description of a dust disk (Dutrey et al. 1996), in the optically thin regime, the flux can be written as:

$$S_\nu(\tau_\nu \ll 1) = \frac{2kT}{D^2}\left(\frac{\nu}{c}\right)^2 \kappa M, \quad (1)$$

where T is the (average) temperature, κ the absorption coefficient, and M the mass (each of these parameters being relative to the gas or dust component).

The continuum emission of dust grains is expected to be optically thin at the considered wavelengths even for proto-planetary disks (typically, the optically thick area has a radius of $R \simeq 10$ au at 1.3 mm for a disk such as that surrounding DM Tau). In contrast, we expect the ^{12}CO gas emission to be mostly in the optically thick regime, where it should then write:

$$S_\nu(\tau_\nu \gg 1) \propto \frac{2\pi kT}{D^2}\left(\frac{\nu}{c}\right)^2 (R_{\rm out}^2 - R_{\rm in}^2) \times \cos(i), \quad (2)$$

where R_{out} and R_{in} are respectively the outer and inner radii of the disk.

To compare the optically thin emission to the optically thick one, we can develop Equation (1) and write the mass as a function of the inner and outer disk radii. Indeed, the mass can be derived from the surface density (see Appendix A.2 for details), $\Sigma(r) = \Sigma_0 \left(\frac{R}{R_0}\right)^{-p}$:

$$M \propto \frac{2\pi\Sigma_0 R_0^2}{2-p}\left(\frac{R_{\rm out}}{R_0} - \frac{R_{\rm in}}{R_0}\right)^{2-p}. \quad (3)$$

At first order, we thus see that the emission in the optically thick regime (upper part of the diagrams), neglecting the inner radius, varies as R_{out}^2, while the optically thin emission varies as R_{out}^{2-p}. The transition between the optically thick and thin regimes for the gas emission should then result in a slope break, as sketched out in Fig. 13. Others parameters, such as the inclination, the difference between the dust and the gas temperatures, or the presence of a large inner hole may be responsible for the dispersion of the points around the global trend in these diagrams, but should not affect the dependence on R_{out}.

Interestingly, we do not observe a break in the correlations of Fig. 7a and 7b, all the observed sources show the same slope suggesting optically thick CO emission all along.

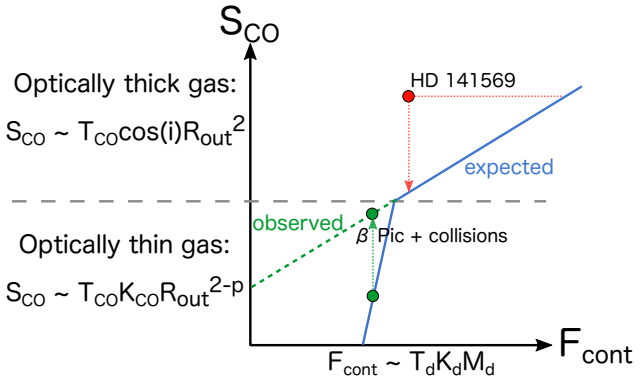

Fig. 13: Diagram showing the physical parameters which dominate the emission of the CO gas and dust (see Section 4.2 for details). The higher part of the plot represents the optically thick regime of the gas, and the lower part represents the optically thin regime. In a hybrid disk such as HD 141569, the dust may evolve faster than the gas in a first step, moving the disk out of the correlation. In a second step, the natural gas dissipation moves downwards in position. On the contrary, debris disks are expected to lie in the optically thin region. For β Pic, the position of the disk in the diagram could be higher than expected because of the gas enhancement produced by collisional events. For both sources, the arrows show the expected path in the diagram resulting from their possible evolutions.

4.2. A possible diagram of evolution

In Figs 7a and 7b , the systems span a large range of properties (luminosity, mass and age etc.), from envelope-embedded young Class II sources to transition and young debris disks, and a large fraction of the disk evolution sequence is represented. Therefore, we investigate whether or not the correlation observed between the CO emission and the thermal mm/sub-mm flux can be interpreted as a sequence of evolution in the life of disks.

First of all, it is important to highlight that the detected hybrid objects are either isolated or in loose associations, and may not be representative of disk evolution in dense clusters. Observations show that the fraction of disks seems lower in older clusters (Haisch et al. 2001; Hernández et al. 2007), which indicates that the disk lifetime is approximately 5 Myr. Survival of disks in general, however, might not be as short as the age determined in these studies. Indeed, in clusters, the rich stellar environment may enhance the disk dispersal and lead to shorter lifetime estimates than for isolated stars (Pfalzner et al. 2014; Vincke et al. 2015). Pfalzner et al. (2014) evaluate that at least 30%, and possibly as much as 50%, of the disks are living for more than 10 Myr. The (isolated) hybrid disks we are discovering nowadays might thus be the first of a long series. The fact

that they are found around isolated A-stars contributes to the ease of their detection, since their disks tend to be more massive and luminous.

Nevertheless, as a proto-planetary disk evolves, its surface density becomes eroded under the effects of viscous evolution, photo-evaporation and planet formation. As a consequence, its dust and gas emissions are expected to decrease until they reach the optically thin domain of debris disks where, for a matter of sensitivity, only the continuum emission of (second generation) dust remains detectable in most cases. The accretion rate is also often interpreted as an indicator of the evolution of the disks, since the accretion signatures are supposed to decrease when the gas dissipates. Hartmann et al. (1998) have identified a decrease of the accretion rates with the stellar age, but the study was restricted to CTTS disks. Several studies have also examined the evolution of the accretion rate in transitional disks compared to CTTS ones, since transitional disks are supposed to be in a more evolved stage than CTTS. It appears that the disk fraction showing accretion signatures is significantly lower in the transitional disk population, but when they are present, the accretion level is similar to the CTTS level, or less than an order of magnitude below (Fang et al. 2013; Sicilia-Aguilar et al. 2010; Espaillat et al. 2012; Najita et al. 2007). Fig. 11 does not show any correlations.

In Figs 7a and 7b, there is no significant difference between young (gas rich) disks orbiting Herbig Ae and T Tauri stars. The linear shape of the CO/grains emission distribution in Figs 7a and 7b, and the small dispersion around the mean trend suggest that the gas and dust components generally evolve concurrently, with comparable dissipation timescales, even if in our sample the distribution of CTTS (including binaries, which are all along the main correlation) is more homogenous than that of Herbig Ae stars.

Although the number of faint disks simultaneously detected in CO line and continuum remains too small for a robust analysis in the bottom-left region of the diagram, all hybrid disk candidates (red symbols) with evolved dust and gas of (partially) primordial origin clearly lie above the correlation line. This reveals either a deficit of dust emission or an excess of CO emission. Similarly, we also observe an enhanced flux ratio in Figs. 8, 9 and 10 for the hybrid disk population.

4.3. Origin of hybrid disks

Herbig Ae stars may follow a different pathway, that is, on a specific trend lying above that of low-mass stars or with a different slope in Figs 7a and 7b, but the lack of Herbig stars in the range $F_{CO} = 10 - 500$ mJy prevents us from drawing conclusions. However, in this region of the diagram, sensitivity is not an issue and the apparent absence of Herbig Ae stars in the vicinity of the hybrid disks group might be better explained by an effect of disk dissipation rather than by a detection bias.

Two scenarios, corresponding to different evolution pathways in Figs 7a and 7b, may be invoked.

4.3.1. Excess of CO by comet/planetesimal destruction

In this first case, dramatic events such as analogs of the Late Heavy Bombardment in our solar system (Gomes et al. 2005) or a massive collision may be invoked to make faint sources move towards the upper part of the diagram. Such a scenario is suspected for β Pictoris, whose large CO intensity is thought to originate from a recent collision between Mars-size objects or in an enhanced collision rate due to planetesimals trapped in mean-motion resonances with an unseen planet (Dent et al. 2014). This suggests that its current location in our diagram, on the same line as optically thick disks, is transient (see Fig. 13), while the "steady-state" regime of the icy debris collisional cascade may produce insufficient CO gas for most debris disks to be detectable (see recent *ALMA* non-detections of CO around the nearby debris disks Fomalhaut and HD 107146, Matrà et al. 2015; Ricci et al. 2015).

For HD 21997, a typical hybrid disk, Kóspál et al. (2013) have evaluated the CO mass from the $C^{18}O$ emission. They constrain it to 4-8$\times10^{-2}$ $M_\oplus$, that is, $\sim4\times10^{23}$ kg and $\sim7\times10^{20}$ kg for ^{12}CO and $C^{18}O$ (assuming an isotopic ratio of 560), respectively. They estimated that such a CO mass cannot be purely produced by cometary collisions, as at least 6,000 Hale-Bopp like comets would need to be totally destroyed each year.

To evaluate the relevance of a comet/planetesimal destruction scenario in explaining the observed CO mass, we outline another approach. We use the following assumptions:

- $M_{disk} = 0.1M_\star = 0.2M_\odot$ for Herbig stars;
- $M_{disk} \approx M_{H_2}$;
- most of the O is in the form of H_2O; the H_2O content of the disk is then given by cosmic oxygen abundance;
- the CO content is derived using a $[CO/H_2O]$ molecular abundance ratio in comets/planetesimals of 10%. This value is found for CO-rich comets such as Hale-Bopp and Lovejoy in the Solar System; the median being ∼4% (see e.g, Paganini et al. 2014; Mumma & Charnley 2011);
- 10% of this CO content ends up locked in comets/planetesimals.
- $X18$, the $^{12}CO/C^{18}O$ ratio in gas and in comets is similar; we use $X18 = 560$.

These assumptions give an estimate of the initial mass of ^{12}CO and $C^{18}O$ in the disk:

$$M_{CO}^{init} < M_{disk} \times m_{O/H} \times \left[\frac{\mathrm{CO}}{\mathrm{H_2O}}\right] \times \frac{m_{CO}}{m_O}, \quad (4)$$

where m_{CO} is the CO molecular mass, m_O the oxygen atomic mass, and $m_{O/H}$ the fraction mass of oxygen compared to H. Taking the cosmic abundance [O/H] = 3.4$\times10^{-4}$ yields $m_{O/H} = 16 \times [O/H] \approx 0.005$. The numerical application gives $M_{CO}^{init} < 4\times10^{26}$ kg. The mass ultimately locked in comets/planetesimals is thus $M_{CO}^{lock} < 4\times10^{25}$ kg and 7×10^{22} kg for ^{12}CO and $C^{18}O$, respectively.

From the observed CO column density in HD 21997, neglecting the shielding from dust grains which have a low column density and taking into account both the stellar UV flux and the ISM flux, Kóspál et al. (2013) found that the lifetime would be $< 30,000$ yr for ^{12}CO and $< 6,000$ yr for $C^{18}O$. The observed $C^{18}O$ content would thus need to be replenished at a rate of 10^{17} kg.yr^{-1}. The available reservoir of comets estimated above would then be exhausted in less than 6×10^5 yr. Without a reservoir, the remaining ^{12}CO would only last <30 000 yr longer.

This should be compared to the required duration of the phenomenon: 3 Myr given the detection rate (approximately 7 %) and age of the oldest system (approximately 40 Myr). Thus, in spite of the uncertainties in our assumptions (particularly in our conservative estimate of the CO production rate), it is very unlikely that the scenario of comets/planetesimals destruction could explain the whole CO emission observed in hybrid disks.

4.3.2. Deficit of mm emission – grain growth

In the second scenario, the observed correlation suggests that disks share common properties during most of their lifetime, differing in characteristic size and surface density, but not in gas to dust ratio, and evolve along the correlation line because of a global decrease in gas and dust content. Hybrid disks would appear when the dust properties change significantly enough to affect the CO flux to mm flux ratio. A potential cause is grain growth, as observed in the inner regions of disks (Guilloteau et al. 2011; Pérez et al. 2012), which lowers the dust opacity and thus the mm flux without affecting the gas. A further reduction of the NIR to UV dust opacity can allow the onset of photo-evaporation, which will then reduce the gas content faster than the dust content (Gorti et al. 2015). In this scenario, the small number of hybrid disks is in accordance with the short duration of the gas-rich, optically thin dust phase.

Unfortunately, the gas to dust ratio is difficult to estimate from the observations, which only prove a high CO to continuum flux ratio in the hybrid disk phase. The more detailed studies of HD 21997 (Kóspál et al. 2013) and HD 141569 (Di Folco et al., in prep.) indicate gas to dust mass ratios much larger than the canonical ISM value of 100 in the outer disk regions ($R >$ 100 au) sampled by the observations. However, the paucity of resolved hybrid disks precludes any firm conclusion on the gas to dust mass ratio, and thus on the validity of the proposed scenario. We note however that a fast dust evolution in these disks around A-type stars is also supported by the observational finding from NIR excess that the (small) dust dispersal timescale was found to be shorter around intermediate-mass stars than around low-mass stars (e.g, Hillenbrand et al. 1993; Kennedy & Kenyon 2009; Ribas et al. 2015).

Current searches have focussed on A stars: establishing the fraction of hybrid disks around lower-mass stars would be an essential step in indentifying the cause of their existence. This requires much more sensitive searches, only possible with ALMA (see Lieman-Sifry et al. 2016). Spatially resolved studies such as those of HD 21997 and HD 141569 are also needed to move from a global CO to dust flux ratio to a view of their respective distributions, and to guide us towards the understanding of this elusive phase.

Acknowledgements. This research has made use of the SIMBAD database, operated at CDS, Strasbourg, France. This publication is based on observations carried out with the IRAM 30-m telescope and the Atacama Pathfinder Experiment (APEX). IRAM is supported by INSU/CNRS (France), MPG (Germany) and IGN (Spain). APEX is a collaboration between the Max-Planck-Institut fur Radioastronomie, the European Southern Observatory, and the Onsala Space Observatory. This work was supported by "Programme National de Physique Stellaire" (PNPS) and "Programme National de Planétologie" (PNP) from INSU/CNRS. Finally, we warmly acknowledge the unknown referee for her/his detailed comments which helped to improve the paper.

References

Abt, H. A. & Levato, H. 1978, PASP, 90, 201
Acke, B., van den Ancker, M. E., & Dullemond, C. P. 2005, A&A, 436, 209
Akeson, R. L. & Jensen, E. L. N. 2014, ApJ, 784, 62
Andrews, S. M., Rosenfeld, K. A., Kraus, A. L., & Wilner, D. J. 2013, ApJ, 771, 129
Andrews, S. M. & Williams, J. P. 2005, ApJ, 631, 1134
Andrews, S. M. & Williams, J. P. 2007, ApJ, 659, 705
Andrews, S. M., Wilner, D. J., Hughes, A. M., Qi, C., & Dullemond, C. P. 2009, ApJ, 700, 1502
Andrews, S. M., Wilner, D. J., Hughes, A. M., Qi, C., & Dullemond, C. P. 2010, ApJ, 723, 1241
Ansdell, M., Williams, J. P., & Cieza, L. A. 2015, ApJ, 806, 221
Augereau, J. C., Lagrange, A. M., Mouillet, D., & Ménard, F. 1999, A&A, 350, L51
Banzatti, A., Testi, L., Isella, A., et al. 2011, A&A, 525, A12
Bary, J. S. & Petersen, M. S. 2014, ApJ, 792, 64
Bast, J. E., Brown, J. M., Herczeg, G. J., van Dishoeck, E. F., & Pontoppidan, K. M. 2011, A&A, 527, A119
Beckwith, S. V. W., Sargent, A. I., Chini, R. S., & Guesten, R. 1990, AJ, 99, 924
Beskrovnaya, N. G., Pogodin, M. A., Miroshnichenko, A. S., et al. 1999, A&A, 343, 163
Binks, A. S. & Jeffries, R. D. 2014, MNRAS, 438, L11
Boccaletti, A., Augereau, J.-C., Marchis, F., & Hahn, J. 2003, ApJ, 585, 494
Boden, A. F., Akeson, R. L., Sargent, A. I., et al. 2009, ApJ, 696, L111
Booth, M., Kennedy, G., Sibthorpe, B., et al. 2013, MNRAS, 428, 1263
Bowler, B. P., Liu, M. C., Kraus, A. L., & Mann, A. W. 2014, ApJ, 784, 65
Breger, M. 1987, ApJ, 319, 754
Brittain, S. D., Rettig, T. W., Simon, T., et al. 2003, ApJ, 588, 535
Brittain, S. D., Simon, T., Najita, J. R., & Rettig, T. W. 2007, ApJ, 659, 685
Brown, J. M., Blake, G. A., Qi, C., et al. 2009, ApJ, 704, 496
Caceres, C., Hardy, A., Schreiber, M. R., et al. 2015, ApJ, 806, L22
Canovas, H., Caceres, C., Schreiber, M. R., et al. 2016, ArXiv e-prints [arXiv:1601.06801]
Carpenter, J. M., Mamajek, E. E., Hillenbrand, L. A., & Meyer, M. R. 2006, ApJ, 651, L49
Carr, J. S., Mathieu, R. D., & Najita, J. R. 2001, ApJ, 551, 454
Castellani, V., Degl'Innocenti, S., Prada Moroni, P. G., & Tordiglione, V. 2002, MNRAS, 334, 193
Chapillon, E., Guilloteau, S., Dutrey, A., & Piétu, V. 2008, A&A, 488, 565
Chapillon, E., Guilloteau, S., Dutrey, A., Piétu, V., & Guélin, M. 2012, A&A, 537, A60
Chen, C. H., Mittal, T., Kuchner, M., et al. 2014, ApJS, 211, 25
Chen, C. H., Sargent, B. A., Bohac, C., et al. 2006, ApJS, 166, 351
Cieza, L. A., Schreiber, M. R., Romero, G. A., et al. 2012, ApJ, 750, 157
Clampin, M., Krist, J. E., Ardila, D. R., et al. 2003, AJ, 126, 385
Czekala, I., Andrews, S. M., Jensen, E. L. N., et al. 2015, ApJ, 806, 154
Czekala, I., Andrews, S. M., Torres, G., et al. 2016, ArXiv e-prints [arXiv:1601.03806]
de Winter, D., van den Ancker, M. E., Maira, A., et al. 2001, A&A, 380, 609
Dent, W. R. F., Greaves, J. S., & Coulson, I. M. 2005, MNRAS, 359, 663
Dent, W. R. F., Thi, W. F., Kamp, I., et al. 2013, PASP, 125, 477
Dent, W. R. F., Wyatt, M. C., Roberge, A., et al. 2014, Science, 343, 1490
Donehew, B. & Brittain, S. 2011, AJ, 141, 46
Duchêne, G., Monin, J.-L., Bouvier, J., & Ménard, F. 1999, A&A, 351, 954
Dutrey, A., Guilloteau, S., Duvert, G., et al. 1996, A&A, 309, 493
Dutrey, A., Guilloteau, S., & Simon, M. 2003, A&A, 402, 1003
Dutrey, A., Wakelam, V., Boehler, Y., et al. 2011, A&A, 535, A104
Duvert, G., Guilloteau, S., Ménard, F., Simon, M., & Dutrey, A. 2000, A&A, 355, 165
Eiroa, C., Marshall, J. P., Mora, A., et al. 2013, A&A, 555, A11
Espaillat, C., D'Alessio, P., Hernández, J., et al. 2010, ApJ, 717, 441
Espaillat, C., Ingleby, L., Hernández, J., et al. 2012, ApJ, 747, 103
Fairlamb, J. R., Oudmaijer, R. D., Mendigutía, I., Ilee, J. D., & van den Ancker, M. E. 2015, MNRAS, 453, 976
Fang, M., van Boekel, R., Bouwman, J., et al. 2013, A&A, 549, A15
Finkenzeller, U. & Mundt, R. 1984, A&AS, 55, 109
Flaherty, K. M., Hughes, A. M., Andrews, S. M., et al. 2016, ApJ, 818, 97
Fukagawa, M., Hayashi, M., Tamura, M., et al. 2004, ApJ, 605, L53
Garcia Lopez, R., Natta, A., Testi, L., & Habart, E. 2006, A&A, 459, 837
Garufi, A., Quanz, S. P., Avenhaus, H., et al. 2013, A&A, 560, A105
Gomes, R., Levison, H. F., Tsiganis, K., & Morbidelli, A. 2005, Nature, 435, 466
Gorti, U., Hollenbach, D., & Dullemond, C. P. 2015, ApJ, 804, 29
Goto, M., Usuda, T., Dullemond, C. P., et al. 2006, ApJ, 652, 758
Grady, C. A., Woodgate, B., Bruhweiler, F. C., et al. 1999, ApJ, 523, L151
Groenewegen, M. A. T., Decin, L., Salaris, M., & De Cat, P. 2007, A&A, 463, 579
Grosso, N., Alves, J., Wood, K., et al. 2003, ApJ, 586, 296
Guilloteau, S., Di Folco, E., Dutrey, A., et al. 2013, A&A, 549, A92
Guilloteau, S., Dutrey, A., Piétu, V., & Boehler, Y. 2011, A&A, 529, A105
Guilloteau, S., Simon, M., Piétu, V., et al. 2014, A&A, 567, A117
Haisch, Jr., K. E., Lada, E. A., & Lada, C. J. 2001, ApJ, 553, L153
Hales, A. S., De Gregorio-Monsalvo, I., Montesinos, B., et al. 2014, AJ, 148, 47
Hardy, A., Caceres, C., Schreiber, M. R., et al. 2015, A&A, 583, A66
Hartigan, P., Edwards, S., & Ghandour, L. 1995, ApJ, 452, 736
Hartigan, P. & Kenyon, S. J. 2003, ApJ, 583, 334
Hartigan, P., Strom, K. M., & Strom, S. E. 1994, ApJ, 427, 961
Hartmann, L., Calvet, N., Gullbring, E., & D'Alessio, P. 1998, ApJ, 495, 385
Hashimoto, J., Tamura, M., Muto, T., et al. 2011, ApJ, 729, L17
Herbig, G. H. & Bell, K. R. 1988, Third Catalog of Emission-Line Stars of the Orion Population : 3 : 1988
Herbst, W. & Shevchenko, V. S. 1999, AJ, 118, 1043
Herczeg, G. J. & Hillenbrand, L. A. 2014, ApJ, 786, 97
Hernández, J., Calvet, N., Briceño, C., Hartmann, L., & Berlind, P. 2004, AJ, 127, 1682

Hernández, J., Calvet, N., Hartmann, L., et al. 2005, AJ, 129, 856
Hernández, J., Hartmann, L., Megeath, T., et al. 2007, ApJ, 662, 1067
Hernández, J., Morales-Calderon, M., Calvet, N., et al. 2010, ApJ, 722, 1226
Hillenbrand, L. A., Massey, P., Strom, S. E., & Merrill, K. M. 1993, AJ, 106, 1906
Howard, C. D., Sandell, G., Vacca, W. D., et al. 2013, ApJ, 776, 21
Hughes, A. M., Wilner, D. J., Kamp, I., & Hogerheijde, M. R. 2008, ApJ, 681, 626
Isella, A., Carpenter, J. M., & Sargent, A. I. 2009, ApJ, 701, 260
Isella, A., Natta, A., Wilner, D., Carpenter, J. M., & Testi, L. 2010, ApJ, 725, 1735
Isella, A., Testi, L., Natta, A., et al. 2007, A&A, 469, 213
Jensen, E. L. N., Mathieu, R. D., & Fuller, G. A. 1996, ApJ, 458, 312
Kastner, J. H., Hily-Blant, P., Sacco, G. G., Forveille, T., & Zuckerman, B. 2010, ApJ, 723, L248
Kastner, J. H., Zuckerman, B., Hily-Blant, P., & Forveille, T. 2008, A&A, 492, 469
Kennedy, G. M. & Kenyon, S. J. 2009, ApJ, 695, 1210
Kennedy, G. M., Murphy, S. J., Lisse, C. M., et al. 2014, MNRAS, 438, 3299
Kiefer, F. 2016, in. prep
Koerner, D. W. & Sargent, A. I. 1995, AJ, 109, 2138
Kóspál, Á., Moór, A., Juhász, A., et al. 2013, ApJ, 776, 77
Kraus, A. L., Ireland, M. J., Cieza, L. A., et al. 2014, ApJ, 781, 20
Kwon, W., Looney, L. W., Mundy, L. G., & Welch, W. J. 2015, ApJ, 808, 102
Lieman-Sifry, J., Hughes, A. M., Carpenter, J. M., et al. 2016, ArXiv e-prints [arXiv:1606.07068]
Luhman, K. L., Allen, P. R., Espaillat, C., Hartmann, L., & Calvet, N. 2010, ApJS, 186, 111
MacGregor, M. A., Wilner, D. J., Andrews, S. M., & Hughes, A. M. 2015, ApJ, 801, 59
Mannings, V. & Emerson, J. P. 1994, MNRAS, 267, 361
Manoj, P., Bhatt, H. C., Maheswar, G., & Muneer, S. 2006, ApJ, 653, 657
Mathews, G. S., Williams, J. P., Ménard, F., et al. 2012, ApJ, 745, 23
Mathieu, R. D., Stassun, K., Basri, G., et al. 1997, AJ, 113, 1841
Matrà, L., Panić, O., Wyatt, M. C., & Dent, W. R. F. 2015, MNRAS, 447, 3936
Matthews, B., Kennedy, G., Sibthorpe, B., et al. 2014, ApJ, 780, 97
Mazoyer, J., Boccaletti, A., Augereau, J.-C., et al. 2014, A&A, 569, A29
McDonald, I., Zijlstra, A. A., & Boyer, M. L. 2012, MNRAS, 427, 343
Meeus, G., Montesinos, B., Mendigutía, I., et al. 2012, A&A, 544, A78
Mendigutía, I., Calvet, N., Montesinos, B., et al. 2011, A&A, 535, A99
Merín, B., Montesinos, B., Eiroa, C., et al. 2004, A&A, 419, 301
Montesinos, B., Eiroa, C., Mora, A., & Merín, B. 2009, A&A, 495, 901
Moór, A., Ábrahám, P., Derekas, A., et al. 2006, ApJ, 644, 525
Moór, A., Ábrahám, P., Juhász, A., et al. 2011, ApJ, 740, L7
Moór, A., Henning, T., Juhász, A., et al. 2015, ApJ, 814, 42
Moór, A., Juhász, A., Kóspál, Á., et al. 2013, ApJ, 777, L25
Mora, A., Merín, B., Solano, E., et al. 2001, A&A, 378, 116
Morales, F. Y., Werner, M. W., Bryden, G., et al. 2009, ApJ, 699, 1067
Mouillet, D., Lagrange, A. M., Augereau, J. C., & Ménard, F. 2001, A&A, 372, L61
Mumma, M. J. & Charnley, S. B. 2011, ARA&A, 49, 471
Munari, U., Dallaporta, S., Siviero, A., et al. 2004, A&A, 418, L31
Najita, J. R., Strom, S. E., & Muzerolle, J. 2007, MNRAS, 378, 369
Natta, A., Testi, L., Muzerolle, J., et al. 2004a, A&A, 424, 603
Natta, A., Testi, L., Neri, R., Shepherd, D. S., & Wilner, D. J. 2004b, A&A, 416, 179
Natta, A., Testi, L., & Randich, S. 2006, A&A, 452, 245
Nilsson, R., Liseau, R., Brandeker, A., et al. 2010, A&A, 518, A40
Öberg, K. I., Qi, C., Fogel, J. K. J., et al. 2010, ApJ, 720, 480
Owen, J. E. & Clarke, C. J. 2012, MNRAS, 426, L96
Paganini, L., Mumma, M. J., Villanueva, G. L., et al. 2014, ApJ, 791, 122
Panić, O., Holland, W. S., Wyatt, M. C., et al. 2013, MNRAS, 435, 1037
Panić, O., van Dishoeck, E. F., Hogerheijde, M. R., et al. 2010, A&A, 519, A110
Pascucci, I., Gorti, U., Hollenbach, D., et al. 2006, ApJ, 651, 1177
Patel, R. I., Metchev, S. A., & Heinze, A. 2014, ApJS, 212, 10
Pecaut, M. J., Mamajek, E. E., & Bubar, E. J. 2012, ApJ, 746, 154
Pérez, L. M., Carpenter, J. M., Chandler, C. J., et al. 2012, ApJ, 760, L17
Perez, S., Casassus, S., Ménard, F., et al. 2015, ApJ, 798, 85
Pericaud, J., Di Folco, E., Dutrey, A., Guilloteau, S., & Pietu, V. 2016, in. prep
Pfalzner, S., Steinhausen, M., & Menten, K. 2014, ApJ, 793, L34
Piétu, V., Dutrey, A., & Guilloteau, S. 2007, A&A, 467, 163
Piétu, V., Dutrey, A., Guilloteau, S., Chapillon, E., & Pety, J. 2006, A&A, 460, L43
Piétu, V., Dutrey, A., & Kahane, C. 2003, A&A, 398, 565
Piétu, V., Guilloteau, S., & Dutrey, A. 2005, A&A, 443, 945
Raman, A., Lisanti, M., Wilner, D. J., Qi, C., & Hogerheijde, M. 2006, AJ, 131, 2290
Reboussin, L., Guilloteau, S., Simon, M., et al. 2015, A&A, 578, A31
Reche, R., Beust, H., & Augereau, J.-C. 2009, A&A, 493, 661
Rhee, J. H., Song, I., Zuckerman, B., & McElwain, M. 2007, ApJ, 660, 1556
Ribas, Á., Bouy, H., & Merín, B. 2015, A&A, 576, A52
Ricci, L., Carpenter, J. M., Fu, B., et al. 2015, ApJ, 798, 124
Ricci, L., Testi, L., Natta, A., et al. 2010, A&A, 512, A15
Ricci, L., Testi, L., Natta, A., Scholz, A., & de Gregorio-Monsalvo, I. 2012, ApJ, 761, L20
Ricci, L., Testi, L., Natta, A., et al. 2014, ApJ, 791, 20
Rigliaco, E., Pascucci, I., Duchene, G., et al. 2015, ApJ, 801, 31
Riviere-Marichalar, P., Barrado, D., Montesinos, B., et al. 2014, A&A, 565, A68
Rizzuto, A. C., Ireland, M. J., & Zucker, D. B. 2012, MNRAS, 421, L97
Roberge, A., Kamp, I., Montesinos, B., et al. 2013, ApJ, 771, 69
Roberge, A. & Weinberger, A. J. 2008, ApJ, 676, 509
Rodriguez, D. R., van der Plas, G., Kastner, J. H., et al. 2015, A&A, 582, L5
Romero, G. A., Schreiber, M. R., Cieza, L. A., et al. 2012, ApJ, 749, 79
Rosenfeld, K. A., Andrews, S. M., Hughes, A. M., Wilner, D. J., & Qi, C. 2013, ApJ, 774, 16
Salter, D. M., Hogerheijde, M. R., & Blake, G. A. 2008, A&A, 492, L21
Salyk, C., Blake, G. A., Boogert, A. C. A., & Brown, J. M. 2011, ApJ, 743, 112
Salyk, C., Herczeg, G. J., Brown, J. M., et al. 2013, ApJ, 769, 21
Salyk, C., Pontoppidan, K., Corder, S., et al. 2014, ApJ, 792, 68
Schneider, A., Song, I., Melis, C., Zuckerman, B., & Bessell, M. 2012, ApJ, 757, 163
Schneider, A., Song, I., Melis, C., et al. 2013, ApJ, 777, 78
Scoville, N. Z., Sargent, A. I., Sanders, D. B., et al. 1986, ApJ, 303, 416
Sheret, I., Dent, W. R. F., & Wyatt, M. C. 2004, MNRAS, 348, 1282
Sicilia-Aguilar, A., Henning, T., & Hartmann, L. W. 2010, ApJ, 710, 597
Simon, M., Dutrey, A., & Guilloteau, S. 2000, ApJ, 545, 1034
Smith, R., Churcher, L. J., Wyatt, M. C., Moerchen, M. M., & Telesco, C. M. 2009, A&A, 493, 299
Stauffer, J. R., Schultz, G., & Kirkpatrick, J. D. 1998, ApJ, 499, L199
Su, K. Y. L., Rieke, G. H., Stansberry, J. A., et al. 2006, ApJ, 653, 675
Sylvester, R. J., Dunkin, S. K., & Barlow, M. J. 2001, MNRAS, 327, 133
Tang, Y.-W., Guilloteau, S., Piétu, V., et al. 2012, A&A, 547, A84
Thi, W.-F., Pinte, C., Pantin, E., et al. 2014, A&A, 561, A50
Thi, W. F., van Dishoeck, E. F., Blake, G. A., et al. 2001, ApJ, 561, 1074
Torres, C. A. O., Quast, G. R., da Silva, L., et al. 2006, A&A, 460, 695
Torres, C. A. O., Quast, G. R., Melo, C. H. F., & Sterzik, M. F. 2008, Young Nearby Loose Associations, ed. B. Reipurth, 757
Torres, G. 2003, Information Bulletin on Variable Stars, 5402
Tsukagoshi, T., Momose, M., Hashimoto, J., et al. 2014, ApJ, 783, 90
Vacca, W. D. & Sandell, G. 2011, ApJ, 732, 8
van Boekel, R., Min, M., Waters, L. B. F. M., et al. 2005, A&A, 437, 189
Vincke, K., Breslau, A., & Pfalzner, S. 2015, A&A, 577, A115
Wade, G. A., Bagnulo, S., Drouin, D., Landstreet, J. D., & Monin, D. 2007, MNRAS, 376, 1145
Walsh, C., Juhász, A., Pinilla, P., et al. 2014, ApJ, 791, L6
Weinberger, A. J., Becklin, E. E., Schneider, G., et al. 1999, ApJ, 525, L53
Weinberger, A. J., Rich, R. M., Becklin, E. E., Zuckerman, B., & Matthews, K. 2000, ApJ, 544, 937
Welsh, B. Y. & Montgomery, S. 2013, PASP, 125, 759
White, R. E. 2003, ApJS, 148, 487
White, R. J. & Ghez, A. M. 2001, ApJ, 556, 265
White, R. J., Ghez, A. M., Reid, I. N., & Schultz, G. 1999, ApJ, 520, 811
Wilking, B. A., Meyer, M. R., Robinson, J. G., & Greene, T. P. 2005, AJ, 130, 1733
Williams, J. P. & Andrews, S. M. 2006, ApJ, 653, 1480
Williams, J. P. & Best, W. M. J. 2014, ApJ, 788, 59
Williams, J. P., Cieza, L. A., Andrews, S. M., et al. 2013, MNRAS, 435, 1671
Wyatt, M. C., Smith, R., Su, K. Y. L., et al. 2007, ApJ, 663, 365
Zhang, K., Isella, A., Carpenter, J. M., & Blake, G. A. 2014, ApJ, 791, 42
Zuckerman, B., Forveille, T., & Kastner, J. H. 1995, Nature, 373, 494
Zuckerman, B. & Song, I. 2004, ApJ, 603, 738
Zuckerman, B. & Song, I. 2012, ApJ, 758, 77

Table 2: ^{12}CO and continuum emission used to plot Tables 7a and 7b. Objects are sorted first by category and then by increasing R.A. Values are presented here as given in the literature. For some rare cases, there are no errorbars. Values in italics correspond to extrapolation from the other frequency. Values given with the symbol "<" followed by an errorbar (e.g. *<1.5 ± 0.5*) correspond to sources observed with ALMA where confusion with surrounding molecular clouds partly affects the emission from the source. Upper limits are 3σ.

ID	Name	CO J=2→1 (Jy.km.s^{-1})	Continuum 1.3 mm (mJy)	CO J=3→2 (Jy.km.s^{-1})	Continuum 0.8 mm (mJy)	References
		CTTS disks				
1	CIDA 1	*0.9 ± 0.8*	*16 ± 8*	1.45 ± 0.05	27 ± 3	1
2	†IRAS 04113+2758	*10 ± 12*	*196 ± 96*	19.1	410 ± 5	2
3	CY Tau	2.02 ± 0.08	111 ± 3	*3.6 ± 1.0*	140 ± 5	3, 4, 5
4	†FQ Tau	*0.2 ± 0.2*	*6 ± 3*	0.239	8.8 ± 1.2	2
5	BP Tau	1.11 ± 0.08	58.2 ± 1.3	*1.90 ± 0.59*	130 ± 7	3, 4, 5
6	RY Tau	6.6	229 ± 17	123 ± 37	560 ± 30	6, 7, 8, 5
7	†FV Tau A	*1.3 ± 1.5*	6.17 ± 0.16	2.17	31 ± 1.4	9, 2
8	†FW Tau c	0.156	3.4 ± 0.2	*0.2 ± 0.1*	*4.9 ± 2.4*	51
9	†FX Tau	*0.9 ± 1.0*	7.1 ± 0.15	1.49	17 ± 0.9	9, 2
10	†DK Tau	*0.9 ± 1.1*	35 ± 7	1.56	66 ± 1.0	9, 2
11	†HK Tau A	*2.3 ± 2.7*	33 ± 0.15	4.1	78 ± 1.1	9, 2
12	†HK Tau B	*1.9 ± 2.2*	12.6 ± 0.15	3.39	57 ± 1.3	9, 2
13	†V710 Tau	*1.8 ± 2.1*	59.18 ± 0.33	3.23	142 ± 1.5	9, 2
14	†GG Tau	*13 ± 16*	*546 ± 298*	53 ± 15	1255 ± 57	8, 5
15	GK Tau A	*2.00 ± 2.33*	5.33 ± 0.56	3.56	15 ± 1	9, 2
16	DL Tau	1.98 ± 0.12	204 ± 2	*3.5 ± 1.1*	440 ± 40	3, 4, 10
17	†HN Tau	*1.4 ± 1.7*	12.8 ± 0.2	2.48	37 ± 1.1	9, 2
18	DM Tau	14.87 ± 0.12	109 ± 2.4	20 ± 6	237 ± 12	11, 4, 8, 5
19	†IT Tau B	*0.6 ± 0.7*	*6.5 ± 3.1*	1.03	10 ± 0.9	2
20	AA Tau	8.2 ± 0.16	88 ± 9	*15.5 ± 4.7*	144 ± 5	11, 5
21	†HO Tau	*0.8 ± 0.9*	17.06 ± 0.27	1.36	38 ± 1	9, 2
22	†HBC 411 B	*0.4 ± 0.4*	5.8 ± 0.27	0.624	14 ± 1	9, 2
23	LkCa 15	13.94 ± 0.15	110 ± 2	23 ± 7	428 ± 11	11, 4, 8, 5
24	J04442713+2512164	*0.6 ± 0.6*	*5.9 ± 3.6*	0.98 ± 0.03	9 ± 2	1
25	†DQ Tau	0.97 ± 0.11	83.1 ± 2.8	*1.7 ± 0.6*	*161 ± 86*	3, 4
26	DR Tau	*49 ± 65*	159 ± 11	103 ± 31	533 ± 7	5, 8
27	†DS Tau	*3.7 ± 4.3*	19.94 ± 0.25	6.69	43 ± 1.4	9, 2
28	GM Aur	19.41 ± 0.11	176 ± 5.3	29.0 ± 8.7	707 ± 4	11, 4, 8, 12
29	V836 Tau	0.84 ± 0.18	24 ± 2	*1.42 ± 0.65*	*42 ± 23*	13
30	†IRAS 05022+2527	*2.9 ± 3.4*	35.22 ± 0.26	5.21	87 ± 1.3	9, 2
31	HD 34282	4.2 ± 0.1	110 ± 10	*7.7 ± 2.2*	*218 ± 131*	2
32	HD 294268	< 0.9	5 ± 0.8	*<1.5 ± 1.8*	19.4 ± 5.4	52
33	V2731 Ori	0.95 ± 0.13	10.7 ± 0.8	*1.6 ± 0.6*	32.6 ± 4.8	52
34	J05391573-0230568	< 2.43	8 ± 1	*<4.3 ± 1.9*	13 ± 2.7	52
35	V602 Ori	0.34 ± 0.08	7.8 ± 0.8	*0.5 ± 0.3*	17.4 ± 4.2	52
36	V606 Ori	0.36 ± 0.07	14.3 ± 0.8	*0.6 ± 0.2*	31.4 ± 4.8	52
37	TWA 34	0.34 ± 0.03	0.54 ± 0.06	*0.55 ± 0.17*	*0.66 ± 0.32*	15
38	TW Hya	12.4 ± 1	540 ± 30	45 ± 4	1620 ± 50	
39	T Cha	*7 ± 7*	81.8	12.46 ± 0.11	198 ± 4	
40	HD 135344	*10 ± 10*	*153 ± 75*	18.6 ± 0.8	314 ± 4.5	16, 17
41	HD 142527	17.4 ± 0.01	1090 ± 0.3	*34 ± 10*	*2700 ± 1500*	18
42	HD 143006	4.28 ± 0.04	43 ± 3	3 ± 1	*78 ± 43*	19, 20, 16
43	J16042165-2130284	*11 ± 11*	*113 ± 53*	21.4 ± 0.2	226 ± 1	21
44	Sz 91	4.93 ± 0.02	40 ± 1	8.55	34.5 ± 2.9	53, 22, 23
45	†AS 205 A (N)	19.23 ± 0.27	377 ± 2	65	905 ± 7	24, 25
46	†AS 205 B (S)	3.02 ± 0.22	64 ± 1	*5.4 ± 1.8*	55 ± 7	24, 25
47	GSS 26	>4	176	*>7.3 ± 19.9*	*364 ± 267*	2
48	GSS 39	>25	304	*>49.9 ± 2.1*	663 ± 3	2, 25
49	WL 18	>0.3	24	*>0.5 ± 1.7*	*42 ± 28*	2
50	WL 14	>0.2	<0.2	*>0.3 ± 1.7*	*<0.2 ± 1.2*	2
51	ISO-Oph 102	*0.3 ± 0.3*	2.9 ± 1.2	0.53 ± 0.05	4.1 ± 0.2	26
52	YLW 16c	>1.6	45	*>2.8 ± 1.8*	*82 ± 58*	2
53	ROX 25	>0.6	29	*>1.0 ± 1.7*	*51 ± 35*	2

Table 2: continued.

ID	Name	CO J=2→1 (Jy.km.s^{-1})	Continuum 1.3 mm (mJy)	CO J=3→2 (Jy.km.s^{-1})	Continuum 0.8 mm (mJy)	References
54	Flying Saucer	>2.1	32	*>3.7 ± 1.9*	*57 ± 39*	2
55	AS 209	7.4	300	16.5	577 ± 3	
56	†V4046 Sgr	11.38 ± 0.16	451 ± 20	*22 ± 7*	*1020 ± 600*	27, 28
			Herbig AeBe disks			
57	†V892 Tau	*22 ± 29*	*293 ± 167*	85.4 ± 26	638 ± 54	8, 5
58	AB Aur	80[1]	103 ± 18	153 ± 4	359 ± 67	2, 5, 16
59	MWC 480	22 ± 0.2	289.3 ± 2.5	52 ± 1.1	*626 ± 336*	11, 4, 16
60	MWC 758	*7.9 ± 8.9*	56 ± 1	15 ± 2	217 ± 40	29, 16, 30
61	HD 245185	0.17 ± 0.03	29 ± 6	*0.3 ± 0.1*	74.1 ± 4.2	14
62	CQ Tau	3.1 ± 0.18	162 ± 2	5.95 ± 0.96	421 ± 9	11, 4, 16, 31
63	HD 100546	*49 ± 62*	*540 ± 272*	158 ± 24	1240	32, 33
64	†AK Sco	2.21 ± 0.01	32.65 ± 0.07	*5.7 ± 1.9*	*52 ± 38*	34
65	HD 163296	46 ± 5	705 ± 12	109 ± 11	1910 ± 20	35, 36
66	HD 169142	2.72 ± 0.7	169 ± 5	32.6 ± 2.5	*349 ± 190*	37, 16
			WTTS disks			
67	J04182147+1658470	<0.09	<0.436	*<0.14*	*<0.53*	38
68	†J04192625+2826142	<0.09	0.533	*<0.14*	*0.66 ± 0.38*	38
69	J04242321+2650084	<0.09	<0.426	*<0.14*	*<0.51*	38
70	J04314503+2859081	<0.09	<0.435	*<0.14*	*<0.53*	38
71	J04325323+1735337	<0.09	<0.438	*<0.14*	*<0.53*	38
72	J04330422+2921499	<0.09	<0.431	*<0.14*	*<0.52*	38
73	J04364912+2412588	<0.09	<0.435	*<0.14*	*<0.53*	38
74	J04403979+2519061	<0.09	<0.431	*<0.14*	*<0.52*	38
75	†J04420548+2522562	<0.09	<0.423	*<0.14*	*<0.51*	38
76	J08413703-7903304	<0.09	<0.476	*<0.14*	*<0.58*	38
77	J08422372-7904030	<0.09	<0.472	*<0.14*	*<0.58*	38
78	J11073519-7734493	<0.09	<0.541	*<0.14*	*<0.67*	38
79	†J11124268-7722230	<0.09	<0.494	*<0.14*	*<0.60*	38
80	†J16002612-4153553	<0.09	0.696	*<0.14*	*0.88 ± 0.5*	38
81	J16010896-3320141	<0.09	<0.442	*<0.14*	*<0.53*	38
82	J16031181-3239202	<0.09	<0.453	*<0.14*	*<0.55*	38
83	†J16085553-3902339	<0.09	1.813	*<0.14*	*2.5 ± 1.5*	38
84	†J16124119-1924182	<0.09	<0.459	*<0.14*	*<0.56*	38
85	†J16220961-1953005	<0.09	<0.483	*<0.14*	*<0.59*	38
86	J16223757-2345508	<0.09	<0.461	*<0.14*	*<0.56*	38
87	J16251469-2456069	<0.09	<0.453	*<0.14*	*<0.55*	38
88	†J16275209-2440503	<0.09	<0.442	*<0.14*	*<0.53*	38
89	†J19002906-3656036	<0.09	0.569	*<0.14*	*0.7 ± 0.3*	38
90	†J19012901-3701484	<0.09	<0.465	*<0.14*	*<0.56*	38
			Hybrid disks			
91	49 Ceti	2 ± 0.3	<2.1	9.5 ± 1.9	8.2 ± 1.9	39, 40
92	HD 21997	2.17 ± 0.23	< 1	2.52 ± 0.27	2.69 ± 0.3	41, 2, 42
93	HD 131835	0.798 ± 0.035	*5.6 ± 4.9*	2.74 ± 0.55	8.5 ± 4.4	54, 43, 44
94	HIP 76310	1,41 ± 0.08	1.2 ± 0.2	*2.4 ± 0.5*	1.6 ± 1.1	54
95	HD 141569	9.57 ± 0.03	3.7 ± 0.4	14.6 ± 1	5.3 ± 0.6	45, 16, 46
96	HIP 84881	1.18 ± 0.04	0.72 ± 0.11	*2.5 ± 1*	*0.7 ± 0.4*	54
			Debris disks			
97	HD 225200	*<1.7 ± 0.5*	–	<3.03	–	2
98	†HD 2772	<0.84	–	*<1.4 ± 1.8*	–	2
99	HD 14055	<0.47	*4.3 ± 2.4*	*<0.8 ± 1.7*	6.4 ± 1.1	2, 47
100	HD 15115	<2.48	2.6 ± 0.6	*<4.4 ± 1.9*	8.5 ± 1.2	2, 48, 47
101	HD 17848	*<5.4 ± 0.5*	–	<10.06	–	2
102	†HD 21620	<0.91	–	*<1.5 ± 1.8*	–	2
103	†HD 23642	0.710 ± 0.18	–	*<1.4 ± 1.8*	–	2
104	HD 24966	*<1.6 ± 0.5*	–	<2.75	–	2
105	HD 30422	*<1.2 ± 0.5*	–	<2.13	–	2
106	HD 31295	<1.1	–	*<1.9 ± 1.8*	–	2
107	HD 35850	*<1.3 ± 0.5*	–	<2.17	<5.4	2

Table 2: continued.

ID	Name	CO J=2→1 (Jy.km.s^{-1})	Continuum 1.3 mm (mJy)	CO J=3→2 (Jy.km.s^{-1})	Continuum 0.8 mm (mJy)	References
108	HD 38206	*<1.5 ± 0.5*	–	<2.67	–	2
109	β Pic	*3.6 ± 3.9*	*34 ± 18*	6.59 ± 0.69	60 ± 6	49
110	HD 42111	<1.21	–	*<2.1 ± 1.8*	–	2
111	HD 54341	*<1.4 ± 0.5*	–	<2.39	–	2
112	HD 71043	*<1.5 ± 0.5*	–	<2.64	–	2
113	HD 71155	*<1.5 ± 0.5*	–	<2.56	–	2
114	HD 78702	*<1.2 ± 0.5*	*0.3 ± 1.9*	<2.03	0.3 ± 2.3	2
115	HD 136246	*<1.4 ± 0.5*	–	<2.37	–	2
116	†HD 159082	<0.66	–	*<1.1 ± 1.8*	–	2
117	HD 164249	*<1.3 ± 0.5*	–	<2.29	–	2
118	HD 166191	*<1.5 ± 0.5*	–	<2.66	–	2
119	HD 181296	*<1.2 ± 0.5*	*9.1 ± 3.7*	<2.11	14.4	2
120	HD 182681	*<1.6 ± 0.5*	*3.4 ± 2.1*	<2.79	5 ± 1.3	2, 47
121	HD 218396	<0.5	20	*<0.8 ± 1.7*	10.3 ± 1.8	2, 50
122	HD 220825	*<1.3 ± 0.5*	–	<2.2	–	2

Notes. [1] The flux of AB Aur is contaminated by the envelope. We have estimated the emission of the disk to be ≈ 80 Jy.km.s^{-1} from interferometric observations with PdBI.
†: binary stars.
References: 1 - Ricci et al. (2014); 2 - this work; 3 - Williams & Best (2014); 4 - Guilloteau et al. (2011); 5 - Andrews & Williams (2005); 6 - Koerner & Sargent (1995); 7 - Beckwith et al. (1990); 8 - Thi et al. (2001); 9 - Akeson & Jensen (2014); 10 - Mannings & Emerson (1994); 11 - Öberg et al. (2010); 12 - Andrews & Williams (2007); 13 - Duvert et al. (2000); 14 - Ansdell et al. (2015); 15 - Rodriguez et al. (2015); 16 - Dent et al. (2005); 17 - Brown et al. (2009); 18 - Perez et al. (2015); 19 - Zuckerman et al. (1995); 20 - Natta et al. (2004b); 21 - Zhang et al. (2014); 22 - Tsukagoshi et al. (2014); 23 - Romero et al. (2012); 24 - Salyk et al. (2014); 25 - Andrews et al. (2009); 26 - Ricci et al. (2012); 27 - Kastner et al. (2008); 28 - Jensen et al. (1996); 29 - Chapillon et al. (2008); 30 - Isella et al. (2010); 31 - Banzatti et al. (2011); 32 - Panić et al. (2010); 33 - Walsh et al. (2014); 34 - Czekala et al. (2015); 35 - Rosenfeld et al. (2013); 36 - Isella et al. (2007); 37 - Raman et al. (2006); 38 - Hardy et al. (2015); 39 - Hughes et al. (2008); 40 - Sheret et al. (2004); 41 - Kóspál et al. (2013); 42 - Moór et al. (2013); 43 - Moór et al. (2015); 44 - Nilsson et al. (2010); 45 -Pericaud et al. (2016); 46 - Sylvester et al. (2001); 47 - Panić et al. (2013); 48 - MacGregor et al. (2015); 49 - Dent et al. (2014); 50 - Williams & Andrews (2006); 51 - Caceres et al. (2015); 52 - Williams et al. (2013); 53 - Canovas et al. (2016); 54 - Lieman-Sifry et al. (2016).

Table 3: Stellar parameters. The classification is the same as in Table 2.

ID	Name	Distance (pc)	Spectral type	$M_\star$ ($M_\odot$)	$L_\star$ ($L_\odot$)	$\dot{M}_{acc}$ ($M_\odot$/yr)	Age Myr	References
			CTTS disks					
1	CIDA 1	140	M5.5	0.13	0.13	–	2.7	1, 2
2	IRAS 04113+2758	140	–	–	–	–	–	
3	CY Tau	140	M1.5	0.44	0.40	4.08×10^{-9}	5	1, 2, 3
4	FQ Tau	140	M3	0.29	0.09	3.55×10^{-7}	6.8	4, 2, 5
5	BP Tau	76.8	K7	0.79	0.97	4.08×10^{-9}	1.7	6, 2, 3
6	RY Tau	192	K1	2.3	21.9	2.24×10^{-8}	3.86	6, 7, 8
7	FV Tau A	140	M5	1.23	2.3	4.79×10^{-8}	3.7	4, 2, 9
8	FW Tau c	140	M9	0.001	–	1.00×10^{-11}	2	48, 49
9	FX Tau	140	M1	0.48	0.52	2.23×10^{-9}	1.7	10, 2, 5
10	DK Tau	140	K8	0.71	1.32	1.05×10^{-9}	1	10, 2, 3
11	HK Tau A	140	M0.5	0.54	0.44	1.95×10^{-9}	2.5	1, 2, 3
12	HK Tau B	140	M2	0.37	0.03	–	4.1	1, 2
13	V710 Tau	140	M0.5	0.54	0.57	–	1.7	1, 2
14	GG Tau	140	K7	1.35	0.85	3.02×10^{-9}	2.1	11, 2, 9
15	GK Tau A	140	K7	0.78	1.35	6.45×10^{-9}	1.1	5, 2
16	DL Tau	140	K7	0.81	0.74	3.22×10^{-8}	2.6	1, 2, 3
17	HN Tau	140	K5	0.91	0.42	2.72×10^{-9}	5.4	12, 2, 3
18	DM Tau	140	M1	0.47	0.23	2.25×10^{-9}	5	5, 2, 3
19	IT Tau B	140	K3	1.41	1.43	–	4.6	10, 2
20	AA Tau	140	K7	0.79	0.87	3.91×10^{-9}	2	5, 2, 3
21	HO Tau	140	M0.5	0.56	0.13	–	13.2	1, 2
22	hbc 411	140	–	–	–	–	–	
23	LkCa 15	140	K5	1.05	0.81	6.77×10^{-10}	3.7	5, 2, 3
24	J04442713+2512164	140	M7.3	–	–	–	–	
25	DQ Tau	140	M0	1.27	0.4	2.53×10^{-9}	3.5	13, 14, 2, 3
26	DR Tau	140	K5	1.2	1.82	1.42×10^{-8}	1.5	1, 2, 3
27	DS Tau	140	K5	1.05	0.76	3.35×10^{-8}	4.1	1, 2, 3
28	GM Aur	140	K3	1.35	1.23	1.21×10^{-8}	5.6	15, 2, 3
29	V836 Tau	140	K7	0.83	0.57	4.20×10^{-9}	3.7	1, 2, 3
30	IRAS 05022+2527	140	M0	–	–	–	–	
31	HD 34282	350	A0	2.35	5.13	$<1.95 \times 10^{-8}$	6.5	50, 19, 40
32	HD 294268	420	F8	–	–	–	–	53
33	V2731 Ori	420	–	–	–	–	–	
34	J05391573-0230568	420	K9	–	–	–	–	53
35	V602 Ori	420	M3	–	–	–	–	53
36	V606 Ori	420	–	–	–	–	–	
37	TWA 34	47	M4.9	–	0.014	–	6	16, 17
38	TW Hya	54	M2.5	0.4	0.19	4.75×10^{-9}	3	18, 3
39	T Cha	164	K0	1.5	–	–	–	
40	HD 135344	140	F3	1.5	7.08	4.27×10^{-8}	8	19, 20
41	HD 142527	140	F6	1.6	7.94	3.55×10^{-8}	8.8	19, 20
42	HD 143006	82	G6	1	0.8	5.11×10^{-9}	>10 00	21, 3
43	J16042165-2130284	145	–	–	–	–	–	
44	Sz 91	200	M2	–	0.25	–	–	17
45	AS 205 A (N)	125	K7	1.5	7.1	7.94×10^{-8}	1.6	22, 23, 24
46	AS 205 B (S)	125	M0.1	0.3	2.19	2.09×10^{-7}	–	17, 23
47	GSS 26	135	M0	0.56	1.39	–	0.5	25, 26
48	GSS 39	135	M1	0.6	1	3.70×10^{-8}	1	27, 24, 28
49	WL 18	135	K7	–	0.3	–	–	29, 30
50	WL 14	135	–	–	–	–	–	
51	ISO-Oph 102	135	M6	0.06	0.08	1.00×10^{-9}	–	31
52	YLW 16c	135	M1	0.48	1.11	–	0.5	25, 26
53	ROX 25	135	–	–	–	–	–	
54	Flying Saucer	120	M1	–	0.14	–	–	32
55	AS 209	125	K5	1.4	2.5	3.02×10^{-8}	0.5	33, 23, 24
56	V4046 Sgr	54	–	–	–	–	–	

Table 3: continued.

ID	Name	Distance (pc)	Spectral type	$M_\star$ ($M_\odot$)	$L_\star$ ($L_\odot$)	$\dot{M}_{acc}$ ($M_\odot$/yr)	Age Myr	References
			Herbig AeBe disks					
57	V892 Tau	140	B8	2.8	38.8	–	46	7, 2
58	AB Aur	139	A1	2.6	51.3	1.41×10^{-7}	3.94	7, 19
59	MWC 480	146	A4.5	1.91	19.1	$<5.89 \times 10^{-8}$	7.1	34, 2, 8
60	MWC 758	279	A3	1.8	17.4	8.90×10^{-7}	3.5	35, 36, 37, 38
61	HD 245185	450	A1	2.2	22.9	–	7.97	7
62	CQ Tau	113	F3	1.6	7.1	$<5.01 \times 10^{-9}$	13.27	7, 8
63	HD 100546	97	B9	2.5	40.7	9.12×10^{-8}	3.46	39, 40, 20
64	AK Sco	103	F5	2.49	–	–	–	41
65	HD 163296	119	A1	2.49	33.9	3.23×10^{-8}	3	19, 40, 20
66	HD 169142	145	A5	2	18.2	3.98×10^{-8}	5.42	19, 40
			WTTS disks					
67	J04182147+1658470	135	K5	–	–	–		
68	J04192625+2826142	135	K7	0.67	–	$< 1.00 \times 10^{-11}$	3.5	42, 43
69	J04242321+2650084	135	M2	0.35	–	$< 1.00 \times 10^{-11}$	6.7	42, 43
70	J04314503+2859081	135	F5	–	–	$< 1.00 \times 10^{-11}$	–	42, 43
71	J04325323+1735337	135	M2	0.36	–	–	3.1	42
72	J04330422+2921499	135	B9	–	–	$< 1.00 \times 10^{-11}$	–	42, 43
73	J04364912+2412588	135	F2	–	–	$< 1.00 \times 10^{-11}$	–	42, 43
74	J04403979+2519061	135	M5	0.17	–	$< 1.00 \times 10^{-11}$	–	42
75	J04420548+2522562	135	K7	0.65	–	–	–	42
76	J08413703-7903304	97	M3	0.27	–	–	3.4	42
77	J08422372-7904030	97	M3	0.31	–	–	15	42
78	J11073519-7734493	160	M4	0.20	–	–	12.4	42
79	J11124268-7722230	160	G8	1.4	–	–	6.9	42
80	J16002612-4153553	150	M5.3	0.17	–	–	26.3	42
81	J16010896-3320141	150	G8	1.1	–	–	7.7	42
82	J16031181-3239202	150	K7	0.7	–	–	2.6	42
83	J16085553-3902339	200	M6	0.1	–	–	6.6	42
84	J16124119-1924182	119	K8	0.64	–	–	2.2	42
85	J16220961-1953005	119	M3.7	0.34	–	–	9.9	42
86	J16223757-2345508	119	M2.5	0.33	–	–	3	42
87	J16251469-2456069	119	M0	0.56	–	–	4.2	42
88	J16275209-2440503	129	K7	0.77	–	–	4.7	42
89	J19002906-3656036	129	M4	0.24	–	–	10.2	42
90	J19012901-3701484	116	M3.8	0.21	–	–	–	42
			Hybrid disks					
91	49 Ceti	59	A1	2.17	21.8	–	8.9	44
92	HD 21997	72	A3	1.8	–	–	30	45
93	HD 131835	122	A2	–	–	–	16	46
94	HIP 76310	151	A0	2.2	26.9	–	10	52, 51
95	HD 141569	116	A0	2.18	22.9	2.24×10^{-8}	6.65	34, 40, 20
96	HIP 84881	118	A0	2.9	15	–	10	51
			Debris disks					
97	HD 225200	129	A0	–	–	–	–	
98	HD 2772	116	B8	–	–	–	–	
99	HD 14055	34	A1	–	–	–	–	
100	HD 15115	45	F2	–	–	–	–	
101	HD 17848	51	A2	–	–	–	–	
102	HD 21620	149	A0	–	–	–	–	
103	HD 23642	139	A0	–	–	–	–	
104	HD 24966	104	A0	–	–	–	–	
105	HD 30422	56	A3	–	–	–	–	
106	HD 31295	36	A0	–	–	–	–	
107	HD 35850	27	F8	1.2	1.78	2.41×10^{-12}	–	3
108	HD 38206	69	A0	–	–	–	–	
109	β Pic	19	A6	–	–	–	20	47
110	HD 42111	201	A3	–	–	–	–	
111	HD 54341	102	A0	–	–	–	–	

Table 3: continued.

ID	Name	Distance (pc)	Spectral type	$M_\star$ ($M_\odot$)	$L_\star$ ($L_\odot$)	$\dot{M}_{acc}$ ($M_\odot$/yr)	Age Myr	References
112	HD 71043	73	A0	–	–	–	–	
113	HD 71155	38	A0	–	–	–	–	
114	HD 78702	84	A0	–	–	–	–	
115	HD 136246	144	A1	–	–	–	–	
116	HD 159082	135	B9	–	–	–	–	
117	HD 164249	48	F6	–	–	–	–	
118	HD 166191	119	F8	–	–	–	–	
119	HD 181296	48	A0	–	–	–	–	
120	HD 182681	69	B9	–	–	–	–	
121	HD 218396	39	A5	–	–	–	–	
122	HD 220825	47	A2	–	–	–	–	

Notes. References: 1 - Luhman et al. (2010); 2 - Andrews et al. (2013); 3 - Rigliaco et al. (2015); 4 - Hartigan & Kenyon (2003); 5 - Hartmann et al. (1998); 6 - Hartigan et al. (1995); 7 - Hernández et al. (2004); 8 - Mendigutía et al. (2011); 9 - White & Ghez (2001); 10 - Duchêne et al. (1999); 11 - White et al. (1999); 12 - Hartigan et al. (1994); 13 - Mathieu et al. (1997); 14 - Czekala et al. (2016); 15 - Espaillat et al. (2010); 16 - Schneider et al. (2012); 17 - Herczeg & Hillenbrand (2014); 18 - Vacca & Sandell (2011); 19 - Garcia Lopez et al. (2006); 20 - Fairlamb et al. (2015); 21 - Natta et al. (2004b); 22 - Bast et al. (2011); 23 - Salyk et al. (2013); 24 - Andrews et al. (2009); 25 - Ricci et al. (2010); 26 - Reboussin et al. (2015); 27 - Natta et al. (2006); 28 - Isella et al. (2009); 29 - Wilking et al. (2005); 30 - Andrews et al. (2010); 31 - Natta et al. (2004a); 32 - Grosso et al. (2003); 33 - Herbig & Bell (1988); 34 - Mora et al. (2001); 35 - Beskrovnaya et al. (1999); 36 - Wade et al. (2007); 37 - Donehew & Brittain (2011); 38 - Meeus et al. (2012); 39 - van Boekel et al. (2005); 40 - Manoj et al. (2006); 41 - Czekala et al. (2015); 42 - Hardy et al. (2015); 43 - Cieza et al. (2012); 44 - Montesinos et al. (2009); 45 - Torres et al. (2006); 46 - Pecaut et al. (2012); 47 - Binks & Jeffries (2014); 48 - Kraus et al. (2014); 49 - Bowler et al. (2014); 50 - Piétu et al. (2003); 51 - Lieman-Sifry et al. (2016); 52 - Hernández et al. (2005); 53 - Williams et al. (2013).
No reference means data comes from SIMBAD.

Appendix A: Mass calculations

Appendix A.1: From integrated flux S_{CO}

From Scoville et al. (1986), the mean column density averaged over the beam writes:

$$N = \frac{k}{h\nu}\frac{3k}{8\pi^3 B\mu^2}\frac{T_x + \frac{hB}{3k}}{(J+1).exp(-\frac{h\nu}{kT_x})}\frac{\tau}{1-e^{-\tau}}\int T_B dv, \quad (A.1)$$

where B is the rotational constant of the observed molecule, μ its permanent dipole moment, J the rotational number of the lower state of the transition, T_x is the excitation temperature, τ the optical depth and T_B the brigntness temperature. This expression assumes the excitation temperature is high compared to the background temperature (see Scoville et al. (1986) for details). The total H_2 mass is related to this column density thanks to the mean atomic weight of the gas μ_G, the dihydrogen mass m_{H_2}, the abundance ratio of CO to H_2 X, the distance of the source D and the beam solid angle Ω_S:

$$M_{H_2} = N\frac{\mu_G m_{H_2}}{X(CO/H_2)}D^2\Omega_S. \quad (A.2)$$

Using the Planck's law, we thus have

$$M_{H_2} = \frac{k}{h\nu}\frac{3cD^2\mu_G m_{H_2}}{16\nu^2\pi^3 B\mu^2 X}\frac{T_x + \frac{hB}{3k}}{(J+1).exp(-\frac{h\nu}{kT_x})}\frac{\tau}{1-e^{-\tau}}.10^{-23}S_{CO}, \quad (A.3)$$

where all terms are in S.I. units, except the integrated flux S_{CO} which should be expressed in Jy.km.s^{-1}. We can sum up by

$$M_{H_2}(M_\oplus) = K_1 \times 10^{-11}\frac{D^2(pc)}{X}\frac{T_x + \frac{hB}{3k}}{exp(-K_2/T_x)}\frac{\tau}{1-e^{-\tau}}S_{CO}. \quad (A.4)$$

For the CO molecule, B = 1.93 cm^{-1} , that is, 5.79×10^{10} Hz, μ = 0.1098 Debye , that is, $\mu^2 = 1.2 \times 10^{-51}$ S.I., and μ_G = 1.36, which implies for the J = 2→1 transition: K_1 = 4.83, K_2 = 11.1 and for the J = 3→2 transition: K_1 = 0.953 and K_2 = 16.6. We have taken the usual value of 10^{-4} for X, the abundance of CO to H_2. In this paper we have set the values of the excitation temperature and opacity to T_{ex} = 40 K and τ = 1.

Appendix A.2: From DiskFit modeling

Error bars on Σ_0 determined by the code DiskFit can be used to determine the H_2 mass as follows:

$$\Sigma_m(r) = \Sigma_0\left(\frac{r}{r_0}\right)^{-p}(cm^{-2}),$$

$$N_{CO} = \int_{r_{int}}^{r_{out}}\int_0^{2\pi}\Sigma_m(r)rdrd\theta,$$

$$N_{CO} = \frac{2\pi\Sigma_0 r_0^2}{2-p}\left(\frac{r_{out}}{r_0}^{2-p} - \frac{r_{out}}{r_0}^{2-p}\right),$$

$$M_{CO} = N_{CO}m_{CO},$$

where Σ_m is the molecular surface density, Σ_0 its value at radius r_0, r_{out} the outer radius of the disk, N_{CO} the number of CO molecules in the disk, m_{CO} the molecular mass of the CO, and M_{CO} the CO mass in the disk (kg). To retrieve the H_2 mass: $X = N_{CO}/N_{H_2} = 1 \times 10^{-4}$, then $N_{H_2} = N_{CO}/X$ and $M_{H_2} = N_{H_2}m_{H_2}$ where N_{H_2} is the number of molecule of H_2, m_{H_2} its molecular mass and M_{H_2} the total mass of H_2.

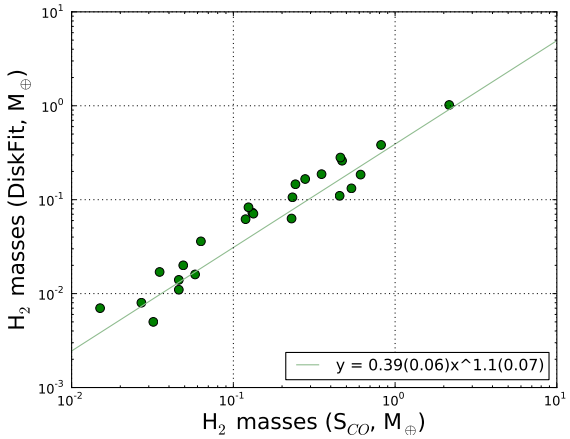

Fig. A.1: Masses of H_2 determined for the debris disks observed with *APEX/IRAM* with the DiskFit method on Y axis and with formula (A.4) on X axis.

Appendix A.3: Comparison of the two methods

The Fig. A.1 presents the masses determined by the two methods. The methods give consistent results within a factor three. The points showing strong deviations are HD 2772, HD 159082 (below the line), and HD 23642 (above the line).

Appendix B: Interpolation of CO and dust emission

Fig. B.1a and B.1b show the correlation between the observations of the continuum and gas emission at the two wavelengths from the literature. A linear regression of the data gives the two following equations, that we have used to fill in the missing values (see section 2.2). When no error is given in the literature, we have assumed a 10% error.

$$S_{CO(3-2)} = 1.7^{\pm 0.4} \times \left(S_{CO(2-1)}\right)^{1.05^{\pm 0.05}}, \quad (B.1)$$

$$F_{cont}^{0.8mm} = 1.3^{\pm 0.5} \times \left(F_{cont}^{1.3mm}\right)^{1.09^{\pm 0.06}}. \quad (B.2)$$

Fig. B.2 shows the correlation between the CO and dust emission, without interpolating the missing values. Only detections of CTTS and Herbig are used to calculate the linear regression. When the error on a measurement was unknown, it was fixed to 20% of the value. A 10% uncertainty was added to those given in Table 2 for the linear regression.

Appendix C: Correlations with stellar parameters

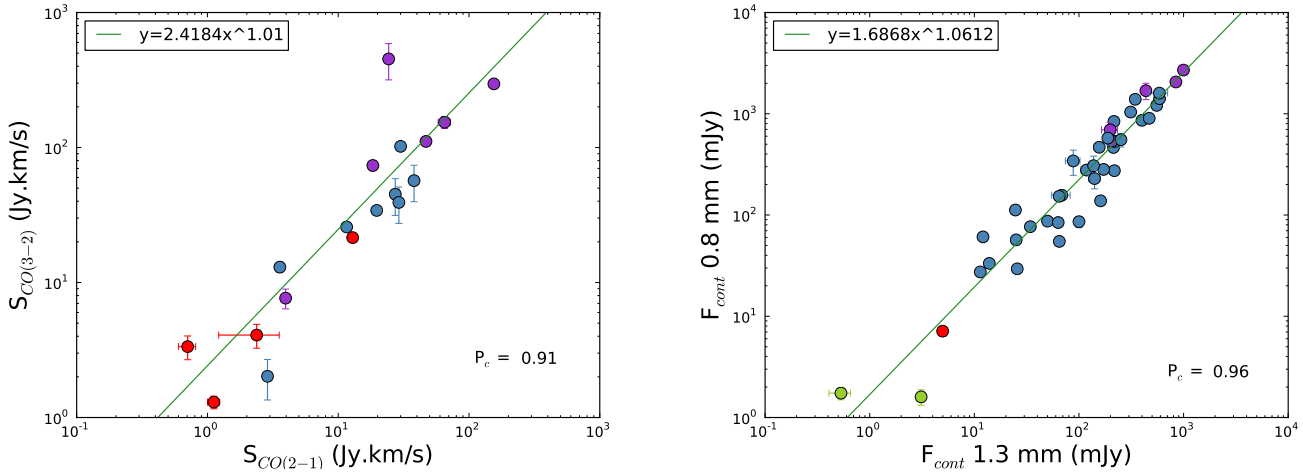

(a) (b)

Fig. B.1: (a) Emission of the CO J=3→2 plotted against the CO J=2→1 emission. The Pearson coefficient of correlation of the data, P_c, is indicated in the lower right-hand corner.
(b) Emission of the continuum at 0.8 mm plotted against the 1.3 mm continuum emission. The Pearson coefficient of correlation of the data, P_c, is indicated in the lower right-hand corner. Fluxes are rescaled at 100 pc. Same symbols as for Fig.B.2

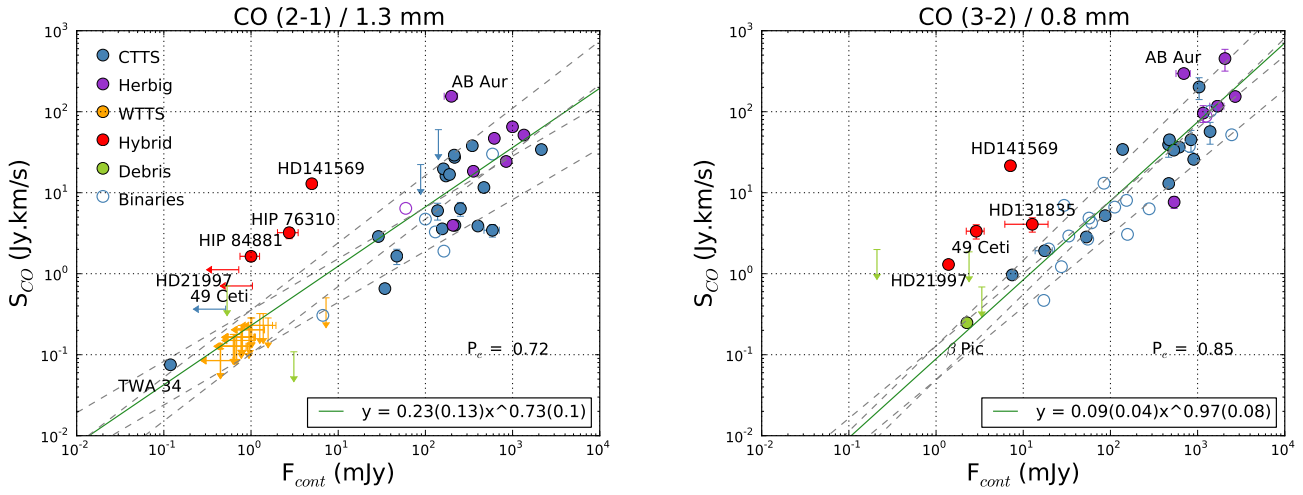

(a) (b)

Fig. B.2: (a) Emission of CO J=2→1 emission plotted against the 1.3 mm continuum emission. The Pearson coefficient of correlation of the data, P_c, is indicated in the lower right-hand corner. No extrapolated data are used here, only observations are reported and used to do the linear regression (green full line, equation indicated in the lower right-hand corner). Right: same as upper left, for the CO J=3→2 emission against the 0.8 mm continuum emission. Fluxes are rescaled at 100 pc.

Table B.1: Ratio of fluxes and derived H_2 masses for sources of the debris disks surveys where CO is detected.

Source	CO(3-2)/CO(2-1)	$M^{32}_{H_2}/M^{21}_{H_2}$
49 Ceti	4.75	1.08
HD 141569	1.68	0.38
HD 21997	1.16	0.26
HD 131835	1.71	0.78

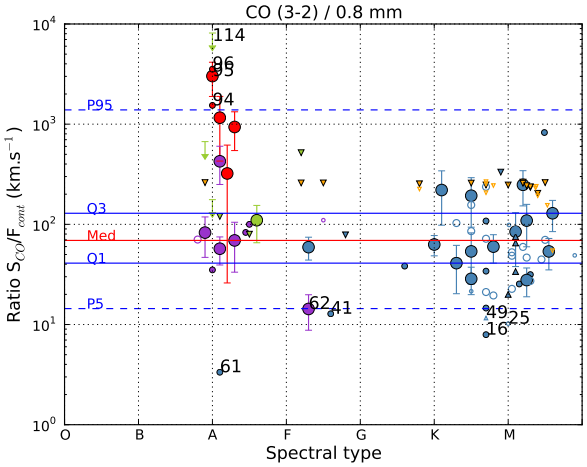

Fig. C.1: Ratio S_{CO}/F_{cont} plotted against the spectral types of the stars, at 0.8 mm. The color code is the same as in Fig. 7a and 7b: blue for CTTS, violet for Herbig, orange for WTTS, red for hybrid and green for debris disks. Some statistics is represented by the lines: the red full line shows the median value of the ratio for the distribution of points, the blue full lines represent the first and third quartiles (50% of the points are between these two lines) and the blue dashed lines shows the 5th and 95th percentiles (90% of the points between the lines).

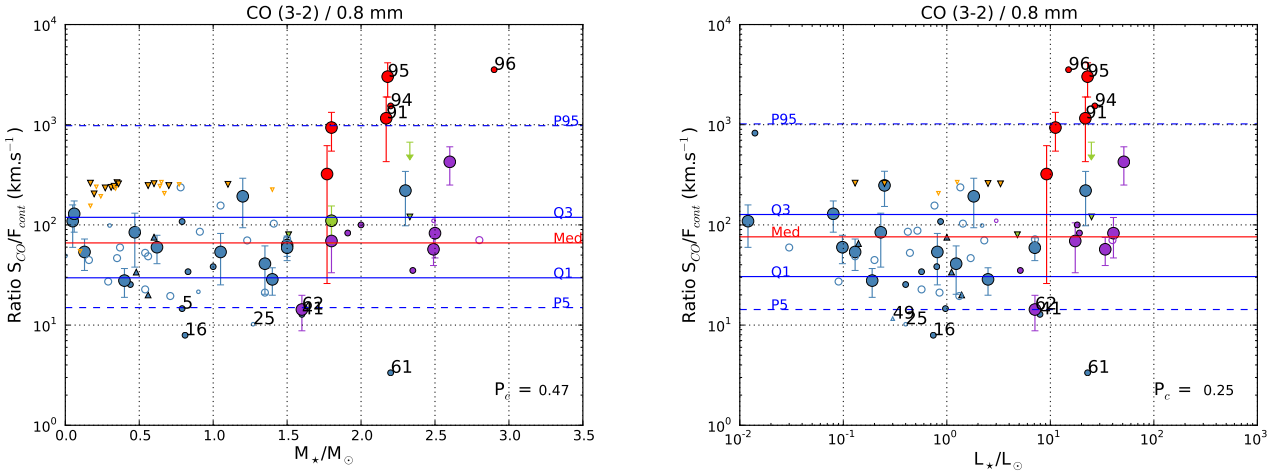

Fig. C.2: Left: Ratio S_{CO}/F_{cont} plotted against the stellar mass, at 0.8 mm. The color code and lines are the same as in Fig. 9. The Pearson coefficient of correlation of the data, P_c, is indicated in the lower right-hand corner. Right: Ratio S_{CO}/F_{cont} plotted against the stellar luminosity, at 0.8 mm. The color code and lines are the same as in Fig. 10. The Pearson coefficient of correlation of the data, P_c, is indicated in the lower right-hand corner.

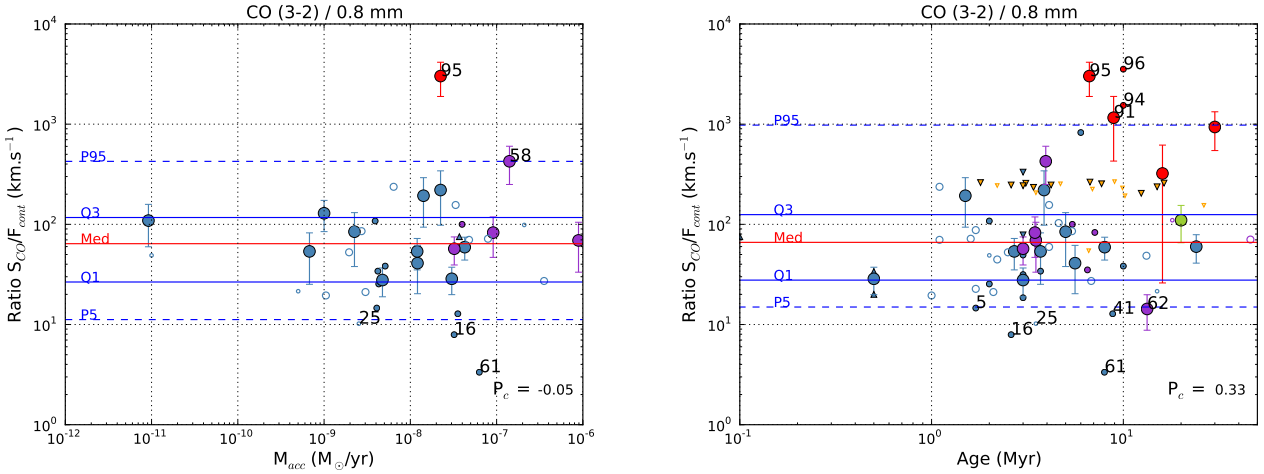

Fig. C.3: Left: Ratio S_{CO}/F_{cont} plotted against the accretion rate, at 0.8 mm. The color code and lines are the same as in Fig. 11. The Pearson coefficient of correlation of the data, P_c, is indicated in the lower right-hand corner. Right: Ratio S_{CO}/F_{cont} plotted against the age of the system, at 0.8 mm. The color code and lines are the same as in Fig. 12. The Pearson coefficient of correlation of the data, P_c, is indicated in the lower right-hand corner.